

1 **CRISPR-ChIP delineates a Menin-dependent oncogenic DOT1L complex in MLL-**
2 **leukaemia**

3

4 Omer Gilan^{1,2,3*}, Charles C. Bell^{1,2}, Laure Talarmain^{1,2}, Daniel Neville³, Kathy Knezevic¹,
5 Daniel Ferguson³, Marion Boudes⁴, Yih-Chih Chan^{1,2}, Chen Davidovich⁴, Enid Y.N. Lam^{1,2},
6 Mark A. Dawson^{1,2,5, 6*}

7

8 ¹Cancer Research Division, Peter MacCallum Cancer Centre, Melbourne, Victoria 3000,
9 Australia

10 ²Sir Peter MacCallum Department of Oncology, University of Melbourne, Victoria 3052,
11 Australia

12 ³Australian Centre for Blood Diseases, Monash University, Melbourne, Victoria, 3004,
13 Australia

14 ⁴Department of Biochemistry and Molecular Biology, Biomedicine Discovery Institute,
15 Monash University, Clayton, Victoria, 3168, Australia

16 ⁵Department of Clinical Haematology, Peter MacCallum Cancer Centre & Royal Melbourne
17 Hospital, Melbourne, Victoria 3000, Australia

18 ⁶Centre for Cancer Research, University of Melbourne, Melbourne, Victoria 3000, Australia

19

20

21 *Corresponding authors.

22

23 Professor Mark A. Dawson
24 Peter MacCallum Cancer Centre,
25 305 Grattan Street, Melbourne, VIC 3000, Australia
26 Email: mark.dawson@petermac.org

27

28 Dr Omer Gilan
29 Australian Centre for Blood Diseases, Monash University,
30 99 Commercial Rd, Melbourne, VIC 3004, Australia
31 Email: omer.gilan@monash.edu

32

33

34 **Summary**

35 The regulation of all chromatin-templated processes involves the selective recruitment of
36 chromatin factors to facilitate DNA repair, replication, and transcription. Chromatin
37 immunoprecipitation (ChIP) is a critical experimental method used to provide spatiotemporal
38 evidence for the coordination of these chromatin-based events including the dynamic
39 regulation of chromatin modifications at cis-regulatory elements. However, obtaining a global
40 appreciation of all the factors that influence a specific chromatin event has remained
41 challenging. Here, as a proof of concept we demonstrate the utility of coupling unbiased
42 functional genomics with ChIP to identify the factors associated with active transcription.
43 Specifically, we use this method to identify the major chromatin factors associated with the
44 catalysis of two evolutionarily conserved histone modifications; H3K4me3 present at the
45 transcriptional start site and H3K79me2 present through the gene body of actively transcribed
46 genes. With CRISPR-ChIP, we identify all the non-redundant COMPASS complex members
47 required for H3K4me3 and demonstrate that RNA polymerase II is dispensable for the
48 maintenance of H3K4me3. As H3K79me2 has a putative oncogenic function in leukaemia cells
49 driven by MLL-translocations, using CRISPR-ChIP we reveal a functional partitioning of
50 H3K79 methylation into two distinct regulatory units. An oncogenic DOT1L complex, where
51 the malignant driver directs the catalytic activity of DOT1L at MLL-Fusion target genes and a
52 separate endogenous DOT1L complex, where catalytic activity is directed by MLLT10. This
53 functional demarcation provides an explanation for the observed synergy with Menin and
54 DOT1L inhibitors and why Menin inhibition surprisingly controls methylation of H3K79 at a
55 critical subset of genes that sustain MLL-fusion leukaemia. Overall, CRISPR-ChIP provides a
56 powerful tool for the unbiased interrogation of the mechanisms underpinning chromatin
57 regulation.

58
59
60
61
62
63
64
65
66
67
68

69 **Introduction**

70 The transcriptional output of every gene is controlled by the cooperative function of chromatin
71 modifiers, transcription factors and transcriptional co-activators. Our ability to unravel this
72 complexity has emerged through a combination of biochemical approaches integrated with
73 genomic assays such as ChIP-seq and RNA-seq¹. However, the genomic assays are limited by
74 the fact that they provide information for a single perturbation at a time. Similarly, as chromatin
75 regulators often function within multi-subunit complexes, the biochemical approaches in
76 isolation, are unable to delineate the precise complex components required for a chromatin-
77 based event, such as a chromatin modification. The opportunity to simultaneously assess the
78 contribution of thousands of proteins in the regulation of a defined chromatin-based event in
79 an unbiased high-throughput manner may provide unique insights and accelerate our
80 understanding of chromatin regulation.

81

82 To address this need we developed a ChIP-based CRISPR screen (CRISPR-ChIP) which
83 enables the concurrent assessment of thousands of nuclear proteins in the coordinated
84 regulation of chromatin. As a proof of principle, we chose to study the regulation of two histone
85 modifications associated with active transcription. H3K4me3 is catalysed by the COMPASS
86 family of methyltransferases and is primarily located over the transcriptional start site (TSS)
87 of actively transcribed genes. In contrast, H3K79me2 is deposited by DOT1L in a non-
88 redundant manner and is predominantly localised throughout the body of the transcribed locus.
89 Notably, H3K79me2 is one of the few histone modifications directly implicated in cancer,
90 specifically MLL-Fusion leukaemias, where several targeted therapies have been specifically
91 developed and clinically translated to inhibit DOT1L and reduce H3K79methylation.
92 Therefore, we sought to focus on this histone modification and study its regulation in MLL-
93 Fusion leukaemia cells.

94

95 Using CRISPR-ChIP, which can couple regulation of chromatin events with a concomitant
96 readout of cell viability, we reveal an unexpected discordance between the functional regulators
97 of H3K79methylation and their essentiality in MLL leukaemia cells. Mechanistically, we
98 demonstrate that underpinning this observation is a functional separation of DOT1L into two
99 complexes in MLL leukaemia cells (i) an endogenous complex containing MLLT10 which
100 deposits H3K79me2 at the majority of expressed genes and (ii) a neomorphic malignant
101 DOT1L complex driven by the MLL-fusion oncogene which localises DOT1L to potentiate
102 gene expression at a subset of target genes required for the maintenance of leukaemia.
103 Additionally, our data provide detailed molecular insights into how Menin inhibitors
104 unexpectedly and selectively influence H3K79methylation at a subset of genes and specify the
105 mechanistic rationale for the synergistic efficacy of Menin and DOT1L inhibition in this
106 disease.

107

108 **Results**

109 **Establishing the CRISPR-ChIP method**

110 Functional genomics using CRISPR screens have provided an unprecedented opportunity to
111 uncover new biological insights in an unbiased manner. Thus far, the majority of CRISPR
112 screening approaches have been restricted to positive and negative selection screens using cell

113 viability as a read out². More recently, these have expanded to FACS-based screens, which
114 enable the selective enrichment of cells expressing a fluorescent protein or cell-surface target
115 that is linked to a specific biological process². As chromatin-based events cannot be easily
116 assessed in this manner we sought to develop CRISPR-ChIP, which directly couples unbiased
117 functional genomics with chromatin immunoprecipitation.

118
119 ChIP involves fragmentation of linker-DNA, which separates neighbouring nucleosomes,
120 using sonication or enzymatic digestion³. Whilst micrococcal nuclease can provide mono-
121 nucleosome resolution, methods that involve sonication of crosslinked chromatin usually result
122 in di- and tri-nucleosome fragments³. Therefore, a key consideration in developing the method
123 was the need to ensure that the integrated guide RNA (sgRNA) sequence remained coupled to
124 the chromatin template that is enriched in a ChIP assay. To address this technical requirement,
125 we chose to link the sgRNA 50-100bp upstream of the regulatory element being assessed in
126 the ChIP assay (**Fig. 1a**).

127
128 To optimise our method, it was important to determine whether the lentivirally integrated
129 regulatory sequences were modified and regulated in a similar manner to the corresponding
130 endogenous loci. Following separate lentiviral infection, we sorted BFP+ cells expressing
131 integrated regulatory sequences representing (i) a strong promoter (*EF1a* promoter), (ii) a weak
132 promoter (*PGK* promoter), (iii) a developmental promoter (*Meis1* promoter) and (iv) the *Myc*
133 enhancer⁴. We then performed ChIP-qPCR, to measure the enrichment of H3K27ac,
134 H3K4me3, H3K9ac, H3K79me2, and Pol II at both the integrated regulatory sequence and the
135 corresponding endogenous locus in human cells. Overall, our results showed that the
136 chromatinised environment surrounding the virally integrated regulatory element undergoes a
137 similar level of histone modification compared to the endogenous locus (**Extended Data Fig.**
138 **1a-d**). Next, we wanted to address if the histone modifications at our integrated reporter were
139 regulated in a similar manner to the endogenous loci. As we were interested in assessing histone
140 modifications associated with active transcription, we chose to use the full (~1kb) *EF1a*
141 promoter and assess H3K27ac and H3K79me2 as the enzymes that deposit these modifications
142 are amenable to inhibition with potent and selective small molecules^{5,6}. This allowed us to
143 assess the changes in the level of these histone modifications around our integrated promoter
144 sequence and the corresponding endogenous locus. We treated cells expressing the integrated
145 *EF1a* promoter sequence with a DOT1L inhibitor (SGC0946) or a P300/CBP inhibitor (A-485)
146 and repeated our ChIP-qPCR analysis. Our data confirmed that treatment of the cells with
147 SGC0946 and A-485 resulted in a marked decrease in H3K79me2 and H3K27ac respectively,
148 at both the integrated promoter sequence and at endogenous genes marked by the histone
149 modifications (**Extended Data Fig. 1e-f**). Together these results suggested that our integrated
150 promoter sequence was subjected to the same epigenetic regulatory processes active at
151 endogenously expressed genes.

152
153 Having established the suitability of the integrated promoter sequence to assess changes in
154 histone modifications associated with gene expression we next sought to validate the ability to
155 discern the depletion of sgRNAs against nuclear proteins that regulate a histone modification
156 of interest. Cognisant of the fact that many chromatin regulators are also common-essential

157 proteins, we wanted to understand if we were able to capture major regulators of a histone
158 modification that were also required for the viability of the cell. To achieve this, we mixed two
159 DOT1L guides with two non-targeting guides and introduced these into leukaemia cells
160 sustained by MLL-AF9 (**Fig. 1b**). We then harvested the cells at both day 2 and day 10 after
161 sgRNA infection. Since H3K79me2 has no known demethylase and we had previously shown
162 that this modification is slowly turned over⁷, we waited until day 10 to perform ChIP for
163 H3K79me2 to allow for marked decrease in H3K79me2 (**Fig. 1b**). To assess the effects on cell
164 viability, we determined the relative guide abundance of the guides at day 10 relative to day 2.
165 As expected, we found that DOT1L guides were depleted in MLL-Fusion leukaemia cells at
166 day 10 (**Fig. 1c and Extended Data Fig. 1g**). To determine the impact on H3K79me2, we
167 performed a ChIP assay at day 10 in viable cells and compared the representation of the
168 sgRNAs from the ChIP sample relative to the input sample at day 10. Here, we see a marked
169 depletion in DOT1L sgRNAs from the H3K79me2 ChIP material, suggesting that in principle,
170 the CRISPR-ChIP method can reliably identify a known epigenetic regulator of a histone
171 modification even when the regulator is required for cell viability (**Fig. 1c and Extended Data**
172 **Fig. 1g**).

173
174 Another important consideration in developing the method to be suitable for a high-throughput
175 screen with a library of thousands of sgRNAs is that the absolute amount of DNA that is
176 immunoprecipitated in a typical ChIP assay can be relatively low (~0.1-10% of the input DNA
177 for the locus of interest). Therefore, unlike conventional CRISPR screening approaches which
178 harvest the entire cellular genomic DNA, the lower yield in this method is a critical parameter
179 that could directly influence the representation of guides in the library. To establish the
180 technical feasibility of the method, we developed a guide RNA library targeting 1144
181 chromatin and transcriptional regulators (each gene was targeted by 6 guides each)
182 (**Supplementary Table 1**). In our workflow (**Fig. 1d**), the lentiviral sgRNA library is infected
183 into cells expressing Cas9; importantly, we aim for a low multiplicity of infection (MOI ~0.3)
184 to ensure that only a single sgRNA is integrated per cell. Therefore, we are only assessing the
185 contribution of genetic depletion of a single chromatin regulator per cell. Expression of BFP
186 from the integrated reporter enables FACS sorting of cells expressing the reporter construct
187 and sgRNA. The viable BFP⁺ cells are then harvested at the desired timepoint and from the
188 same population of cells, we apportion one sample to provide us with the input library, while
189 the remaining cells are cross-linked, sonicated and taken forward in a standard ChIP assay for
190 the target of interest (**Fig. 1d**). Both input and ChIP samples are then assessed by next-
191 generation sequencing (NGS) for the depletion or enrichment of guides (using MAGECK) in
192 the ChIP sample relative to input.

193
194 To assess the cell number required to reliably retain library representation, we performed
195 CRISPR-ChIP for H3K27ac from Cas9 negative K562 cells. Since no gene editing occurs, we
196 could determine the extent to which library representation is altered in the ChIP sample
197 (relative to the input library) from different starting cell numbers. Our results revealed that
198 library representation following lentiviral infection was very highly correlated between two
199 independent replicates of the input library (**Fig. 1e**). Importantly, we also found that the two
200 independent replicates of H3K27ac ChIP were highly correlated (**Fig. 1e**). Notably, an

201 excellent correlation in the representation of the sgRNA library between the ChIP and input
202 samples was faithfully maintained from 100 million cells ($r=0.985$) down to 5 million cells
203 ($r=0.958$) (**Fig. 1e and Extended Data Fig. 2a**). As ChIP efficiency is dependent on the quality
204 of the antibody and abundance of the target of interest, we wanted to use our data to model the
205 point at which technical limitations in the ChIP could result in substantial skewing in library
206 representation. To address this, we performed *in silico* down sampling of the H3K27ac ChIP
207 sample and plotted the guide representation density. This analysis revealed that substantial
208 skewing only begins to occur when the ChIP sample contains less than 50-fold representation
209 of each sgRNA within the library (**Fig. 1f**).

210

211 The change in abundance of histone modifications is not binary and instead spans a continuous
212 spectrum, we therefore wanted to understand whether CRISPR-ChIP has sufficient sensitivity
213 to capture a quantitative change in the levels of the modification. To achieve this, we infected
214 separate Cas9 negative K562 cells with either a human or mouse guide library and treated the
215 cells harbouring the human library with a DOT1L inhibitor (SGC0946) for up to 96hrs. In
216 parallel, we treated the cells containing the mouse library with vehicle (DMSO). The mouse
217 and human K562 cells were then mixed at 1:1 ratio and the relative guide enrichment from the
218 ChIP for H3K79me2 were determined at various timepoints. This approach allowed us to
219 compare the enrichment of the CRISPR library from SGC0946 treated cells where there is a
220 gradual and progressive reduction in H3K79me2 (**Fig. 1g**) compared to vehicle treated cells
221 where the modification stays constant. Our results showed that the CRISPR-ChIP for
222 H3K79me2 in the treated/vehicle (human/mouse) mix accurately reflected the input guide
223 distribution and enrichment (**Fig. 1h**). Furthermore, we clearly observed a quantitative time-
224 dependent reduction in the representation of the human library with our ChIP for H3K79me2
225 following SGC0946 treatment relative to the vehicle treated mouse library (**Fig. 1h**). Notably,
226 these data closely parallel the change in abundance noted by western blot (**Fig. 1i**). Together
227 these data serve to highlight the fact that CRISPR-ChIP can detect a quantitative alteration in
228 the level of a chromatin modification. Finally, we also performed MAGECK analysis on the
229 CRISPR-ChIP data from Cas9 negative cells to determine the expected background scores
230 generated by the method when no editing occurs (**Extended Data Fig. 2b**). This control
231 analysis revealed the low probability of false positives arising from CRISPR-ChIP providing
232 further confidence that our method was robust.

233

234 **CRISPR-ChIP identifies the major non-redundant regulators of H3K4me3.**

235 The tri-methylation of lysine 4 on histone H3 (H3K4me3) is one of the best characterised
236 histone modifications, as it is invariably localised at the transcription start site of actively
237 transcribed genes in all eukaryotes and its abundance is directly correlated with transcriptional
238 activity at the locus^{8,9}. The yeast model organism *Saccharomyces cerevisiae* has a single
239 methyltransferase, SET1, that deposits this modification. However, in mammals there are six
240 H3K4 methyltransferases (SET1A/B and MLL1-4), which have all been shown to strongly
241 associate with the initiated form of RNA polymerase II (Pol II)^{10,11}. Of these, SET1A/B are
242 thought to be the methyltransferases responsible for the majority of H3K4me3¹², whereas,
243 MLL1/2 deposit H3K4me3 at key developmental genes¹³. The methyltransferases in isolation
244 are not efficient enzymes at depositing H3K4me3, instead their catalytic activity is almost

245 entirely dependent on their incorporation into a multi-subunit protein complex called
246 COMPASS (containing either SET1A/B) or COMPASS-like (containing one of MLL1-4). The
247 various subunits of the COMPASS and COMPASS-like complexes are essential for the
248 stability and functional integrity of the methyltransferases.

249

250 To uncover the non-redundant functional regulators of H3K4me₃, the prototypical histone
251 modification associated with active transcription, we performed CRISPR-ChIP for H3K4me₃
252 in K562 cells (**Fig. 2a and Supplementary Table 2**). The top hits in our screen were the four
253 proteins commonly referred to as WRAD (**Fig. 2b**), including WD repeat-containing protein 5
254 (WDR5), Retinoblastoma Binding Protein 5 (RBBP5), Absent-Small-Homeotic-2-Like
255 protein (ASH2L) and Dumpy-30 (DPY30)¹⁴. The four WRAD components are fundamental
256 core proteins that comprise all COMPASS and COMPASS-like complexes and are known to
257 be required for the functional integrity of COMPASS and COMPASS-like complexes, which
258 deposit and maintain of H3K4me₃^{13,14}. In line with the results of the CRISPR-ChIP screen, we
259 subsequently validated that CRISPR-Cas9 mediated deletion of ASH2L or RBBP5 resulted in
260 a global loss of H3K4me₃ by western blot and ChIP-seq (**Fig. 2c-e and Extended Data Fig.**
261 **2c**). Consistent with the fact that there is significant redundancy between the catalytic orthologs
262 SETD1A/B, MLL1/2 and MLL3/4, none of these H3K4 methyltransferase enzymes were
263 identified in our screen. However, the screen did identify CXXC1 and WDR82 that are specific
264 subunits of the mammalian SETD1A/B COMPASS complex (**Fig. 2a-b**). These findings are
265 entirely consistent with biochemical and cell biology studies showing that loss of CXXC1 and
266 WDR82 is followed by a very specific global loss of H3K4me₃ and not H3K4me₁ or
267 H3K4me₂¹⁵⁻¹⁷. A further testament to the validity of this screening approach is the fact that we
268 also identified several members of the mammalian PAF complex which has been carefully
269 characterised through various biochemical approaches in *S. cerevisiae* and shown to interact
270 with Pol II to provide a scaffold for the COMPASS complex and consequent deposition of
271 H3K4me₃¹⁸.

272

273 **Loss of RNA Pol II does not alter global levels of H3K4me₃**

274 The reciprocal interplay between Pol II and H3K4me₃ has been the subject of intense debate¹⁹⁻
275 ²¹. It has been proposed that rather than being instructive for transcription, H3K4me₃ may be
276 a consequence of it, and instead, plays a key role in influencing transcriptional consistency²²
277 and regulating co-transcriptional events such as splicing and termination of transcription^{23, 24}.
278 In this regard, a striking observation from the screen was the clear absence of Pol II subunits
279 and the general transcriptional machinery (**Fig. 2a**). To assess whether these are false negative
280 hits, we independently verified the finding that loss of Pol II did not affect global levels of
281 H3K4me₃ by depleting the major subunit of Pol II, Rpb1, using two independent sgRNAs.
282 Western blot analysis revealed that depletion of Rpb1 did not impact the global levels of
283 H3K4me₃ (**Fig. 2f**). As a distinct control, we included H3K27ac, another dynamic and rapidly
284 turned over histone modification associated with gene activity. Here again, we found that loss
285 of Rpb1 did not affect global levels of H3K27ac (**Fig. 2f**). To confirm these results with an
286 orthogonal approach, we performed ChIP-seq for both Pol II, H3K4me₃ and H3K27ac after
287 depletion of Rpb1. These data again confirm that H3K4me₃ and Pol II levels at TSS are highly
288 correlated in the control cells (**Extended Data Fig. 2d**). Furthermore, as expected, depletion

289 of Pol II by CRISPR-mediated knockout of Rpb1 resulted in a profound reduction of Pol II at
290 chromatin (**Fig. 2g-h**). However, again we found that the dramatic loss of chromatin bound Pol
291 II had a negligible effect on H3K4me3 genome-wide (**Fig. 2i**).

292

293 It has been suggested by studies in yeast that H3K4me3 levels can persist for several hours
294 after transcription ceases²⁵. Therefore, to ascertain whether the retention in H3K4me3 levels
295 after Pol II deletion is also seen with other histone modifications associated with active
296 transcription, we also performed ChIP-seq for H3K27ac following Pol II depletion. Consistent
297 with our observations for H3K4me3, Pol II was also not required for the genome-wide
298 maintenance of H3K27ac (**Fig. 2j**). Taken together, these results suggest that although
299 H3K4me3 is strongly associated with active transcription, a global decrease in chromatin
300 bound Pol II has little influence on H3K4me3 levels.

301

302 **MLLT10 and global H3K79me2 are dispensable for survival of MLL-Fusion leukaemia** 303 **cells**

304 We were encouraged by the fact that in a single experiment, CRISPR-ChIP had identified most
305 of the known regulators of H3K4me3. Therefore, we next wanted to apply the CRISPR-ChIP
306 approach to study the regulation of a histone modification closely associated with the
307 maintenance of malignant gene expression in a unique cancer setting, leukaemias driven by
308 MLL-fusion oncogenes²⁶. H3K79 lies in the globular domain of histone 3 and unlike
309 H3K4me3, which is deposited by multiple enzymatic subunits, H3K79methylation is known
310 to be globally regulated by a single enzyme, which in mammals is DOT1L²⁷. H3K79me2 is
311 distributed throughout the coding region of actively transcribed genes, where it is thought to
312 play a role in facilitating transcription. Previous proteomic and biochemical studies have shown
313 that the endogenous DOT1L complex is comprised of DOT1L, MLLT10, MLLT1/ENL and
314 MLLT6/AF17^{7,28} (**Extended Data Fig. 3a**). Moreover, whilst MLLT1/ENL is also found in
315 the P-TEFb/super elongation complex (SEC), the other components of the DOT1L complex
316 (DOT1L, MLLT10 and MLLT6) are mutually exclusive with P-TEFb/SEC²⁸⁻³⁰. On the other
317 hand, in leukaemia cells containing an MLL-Fusion oncogene, DOT1L has been shown to be
318 recruited by MLL-Fusion partners to increase H3K79methylation at critical MLL-Fusion target
319 genes associated with leukaemia development³¹⁻³⁴. Whilst DOT1L activity in MLL-Fusion
320 leukaemia has been intensively studied³⁵, the relative contribution of the MLL-Fusion
321 oncogene to the regulation of H3K79me2 and whether there are other major regulators of this
322 histone modification remains unclear.

323

324 To address these questions, we performed a CRISPR-ChIP screen for H3K79me2 in MLL-AF9
325 leukaemia cells. Our results clearly identified DOT1L and MLLT10 but not the other DOT1L
326 complex members as key non-redundant regulators of H3K79me2 (**Fig. 3a and**
327 **Supplementary Table 3**). Early biochemical studies in yeast established the importance of
328 H2Bub for the methylation of H3K79 by DOT1L³⁶⁻³⁸ and more recently the mammalian ring
329 finger protein 20 (RNF20), the major H2B ubiquitin ligase, was shown to be required for the
330 maintenance of H3K79me2 and the DOT1L mediated malignant gene expression program in
331 MLL-AF9 leukaemia cells³⁹. In line with these findings, CRISPR-ChIP also identified RNF20
332 as a major non-redundant regulator of H3K79me2 (**Fig. 3a**). Whilst the PAF complex is known

333 to be required for efficient deposition of H3K79me2, our CRISPR-CHIP data specifically
334 identified RTF1, which in contrast to its role in yeast, is a labile PAF complex subunit in
335 mammalian cells where it functions to markedly potentiate transcriptional elongation^{40,41}.
336 Interestingly, recent structural studies have suggested that the stimulation of Pol II elongation
337 by RTF1 depends on its interaction with other components of the Pol II elongation complex
338 particularly DSIF⁴¹. Notably, our CRISPR-ChIP screen identified both components of DSIF
339 (SUPT4H1 and SUPT5), Iws1 (Supt6h), Tceb3 (Elongin A) and Ints3 (**Fig. 3a**), which are all
340 known to function as potentiators of Pol II elongation⁴¹⁻⁴³. Although, H3K79me2 has been
341 loosely associated with transcriptional elongation, functional experimental evidence linking
342 H3K79me2, and Pol II elongation has been scarce. Rather remarkably, our functional genomics
343 approach identified the key subunits of the (i) PAF-complex⁴⁴, (ii) DSIF complex⁴⁵, (iii)
344 Elongin complex⁴⁶ and (iv) Integrator complex⁴⁷, which have all been functionally validated to
345 affect pause release and Pol II elongation rate^{48,49}. These results strongly support the notion
346 that the maintenance of H3K79me2 by the DOT1L complex is dependent on efficient Pol II
347 elongation.

348
349 As our CRISPR-ChIP approach was designed to enable us to uncouple the regulation of
350 H3K79me2 from the requirement for malignant cell viability, we next wanted to assess which
351 of the major regulators of H3K79me2 were also required for the survival of the MLL-AF9
352 leukaemia cells. As expected, many of the components required for Pol II elongation are
353 common essential proteins and similarly, RNF20 and DOT1L which are established
354 dependencies in MLL-AF9 leukaemia, also read out in our viability screen (**Fig. 3b and**
355 **Supplementary Table 4**). Surprisingly, while MLLT10 is known to recruit DOT1L to
356 chromatin via its PZP domain⁵⁰ and clearly reads out as being required for H3K79me2 levels,
357 it did not appear to be required for leukaemia cell survival (**Fig. 3b and Extended Data Fig.**
358 **3b**). To investigate these unexpected findings further we initially used two independent
359 sgRNAs against each of the components of the DOT1L complex and assessed the effects on
360 both global H3K79me2 levels and cell survival in MLL-AF9 leukaemia cells. These data
361 confirmed that loss of DOT1L results in a global depletion of H3K79me2 and also dramatically
362 reduces the survival of MLL-AF9 leukaemia cells^{6,51} (**Fig. 3c-d**). Moreover, we also validated
363 previous results showing that ENL is a dependency in MLL-AF9 leukaemia^{52,53} but does not
364 alter global H3K79methylation levels (**Fig. 3c-d**). Notably however, we confirmed that loss of
365 MLLT10 has a profound effect on global H3K79me2 levels, but this is not accompanied by a
366 survival disadvantage for the leukaemia cells (**Fig. 3c-d**). These findings are recapitulated in
367 the Dep-Map database where all the MLL-leukaemia cell lines show a dependency on ENL for
368 survival but only the cell lines, MOLM13 and MOLM14, both derived from the same patient,
369 and SHI-1 (MLL-AF6), which does not aberrantly recruit DOT1L, show a dependency on
370 MLLT10 (**Fig. 3e**). To explore the functional consequences of depletion of the four members
371 of the DOT1L complex, we performed RNA-seq analysis following CRISPR/Cas9 deletion
372 of each complex member (**Extended Data Fig. 3a-c**). When we analyse the top 100 genes
373 downregulated by DOT1L loss, we also see a concomitant modest decrease in expression of
374 these genes after depletion of ENL (**Fig. 3f**). Strikingly however, the genes most affected by
375 DOT1L loss in MLL-AF9 leukaemia cells do not change their expression when either MLLT10
376 or MLLT6 are depleted (**Fig. 3f and Extended Data Fig. 3c-e**). Together, these surprising

377 findings raise the prospect that although DOT1L is critical, global H3K79methylation levels
378 maybe dispensable in MLL leukaemia and highlight our incomplete understanding of the
379 regulation of H3K79methylation in this disease.

380

381 **Selective regulation of transcription by MLL-AF9**

382 In order to address the discrepancy between H3K79me2 regulation and leukaemia cell survival
383 by MLLT10 and DOT1L, we first sought to determine the influence of the MLLAF9 oncogene
384 on both H3K79methylation and transcription of its direct target genes.

385

386 Current approaches for assessing the transcriptional influence of chromatin proteins largely
387 rely on coupling methods to map chromatin occupancy (such as ChIP-seq) with changes in
388 transcriptional output (using various RNA-Seq methods) following a perturbation of the target
389 of interest¹. However, in the absence of small molecule inhibitors, the slow kinetics of genetic
390 depletion experiments (e.g. shRNA/CRISPR) hampers the accurate assessment and separation
391 of primary and secondary transcriptional changes. These limitations can be overcome by
392 genetically engineered approaches that hijack the endogenous protein degradation machinery
393 for rapid degradation of the target of interest by small molecules⁵⁴⁻⁵⁶. We adopted this system
394 by generating a murine retroviral model of MLL-AF9 leukaemia engineered to contain a
395 3xFLAG tag for efficient mapping by ChIP-seq and a minimal auxin inducible degron (mAID)
396 for rapid degradation using the plant hormone, auxin (IAA)⁵⁵. To ensure that the MLL-AF9-
397 F3-mAID construct faithfully recapitulated the disease biology induced by MLL-AF9, we
398 transplanted our *in vitro* transformed haematopoietic stem and progenitor cells (HSPC) into
399 C57/BL6 mice (**Fig. 4a**). We generated both MLL-AF9-F3-mAID and MLL-AF9-F3-mAID +
400 mutant NRAS transformed cells and showed that both genotypes engrafted and gave rise to
401 fulminant leukaemia with the expected disease latency (**Extended Data Fig. 4a**). To determine
402 the genome-wide occupancy of MLL-AF9, we performed FLAG ChIP-seq in biological
403 duplicates from MLL-AF9-F3-mAID along with ChIP-seq for Menin and H3K79me2 as well
404 as a FLAG ChIP-seq from non-FLAG tagged MLL-AF9 transformed cells as a negative control
405 (**Fig. 4b-c and Extended Data Fig. 4b-c**). The MLL-AF9-F3-mAID ChIP-seq data shows a
406 high level of enrichment at previously reported MLL-AF9 target genes (e.g., Meis1 and Hoxa9)
407 (**Fig. 4d and Extended Data Fig. 4b-c**). Notably, genes bound by MLL-AF9 were also co-
408 occupied by Menin and H3K79me2, with all three factors displaying highly correlated
409 enrichment (**Fig. 4c-d**).

410

411 To determine the genes directly regulated by MLL-AF9, we treated MLL-AF9-F3-mAID cells
412 expressing the plant Tir1 E3 ligase gene with indole-3-acetic acid (IAA) to facilitate IAA-
413 dependent degradation of MLLAF9 (**Fig. 1e**). Time course analysis of MLL-AF9-F3-mAID +
414 Tir1 cells treated with IAA showed near complete degradation within 2-4 hours of treatment
415 (**Fig. 4f**). MLL-AF9 degradation resulted in a marked proliferation arrest and induction of
416 differentiation, consistent with the role of MLL-AF9 in the maintenance of the leukaemic
417 state⁵⁷ (**Extended Data Fig. 4d-e**). To then identify the direct targets of MLL-AF9, we treated
418 cells for 2hrs with IAA and performed FLAG ChIP-seq for MLLAF9-F3-mAID and nascent
419 RNA-seq (4su-seq). FLAG ChIP-seq showed a dramatic global loss of MLL-AF9 from
420 chromatin; however, nascent RNA-seq uncovered a core set of genes (Padj < 0.05) representing

421 only ~2% (260/10221) of the genes bound by MLL-AF9 that were immediately downregulated
422 following MLL-AF9 degradation (**Fig. 4g-h and Extended Data Fig. 4f-h**). To complement
423 the nascent RNA-seq data we also performed ChIP-seq for RNA polymerase II phosphorylated
424 on serine 2 (RNA-PolIIS2ph). While we observed a global loss of MLL-AF9 from chromatin
425 following 2hrs of degradation, global levels of RNA-PolIIS2ph were largely unchanged
426 (**Extended Data Fig. 4i**). However, in agreement with the nascent RNA-seq data, we observed
427 a selective loss of RNA-PolIIS2ph only at the MLL-AF9 bound genes that change their
428 expression 2 hours after degradation of the oncoprotein (**Fig. 4i-j and Extended Data Fig. 4j**).
429 Taken together, these data illustrate that the chromatin localisation of the oncoprotein is
430 insufficient in isolation to assign a regulatory influence on transcription and emphasises the
431 fact that although a large number of active genes are bound by MLL-AF9, only a small subset
432 of these are fully reliant on the MLL-FP for their expression.

433

434 **MLL-AF9 selectively influences H3K79methylation at distinct target genes**

435 Recently published data revealed that inhibition of either Menin or DOT1L with small
436 molecule inhibitors effectively evicted MLL-AF9 from chromatin⁵⁶ (**Fig. 5a**). However, the
437 converse, which is the impact of global MLLAF9 eviction on H3K79methylation was not
438 comprehensively assessed. Indeed, we confirmed the previous reports that both Menin
439 (VTP50469) and DOT1L (SGC0946) inhibition caused the global eviction of MLL-AF9 from
440 chromatin after 48 and 72hrs of treatment, respectively (**Fig. 5b, d and Extended Data Fig.**
441 **5a**). Nonetheless, a major conundrum when assessing the chromatin localisation of
442 transcriptional activators is that it is often hard to distinguish whether displacement of the
443 regulator from chromatin is simply a consequence of a decrease in transcription. Despite,
444 numerous studies assessing the transcriptional effects of MLL fusion proteins such as MLL-
445 AF9, none have specifically addressed or answered this important issue. To resolve this issue,
446 we decided to rapidly degrade the BET bromodomain proteins as targeting these proteins has
447 previously been shown to be effective in MLL leukaemia cells^{58,59} and rapid degradation leads
448 to a profound and global loss of transcription^{60,61}. Remarkably, we found that even after 8 hours
449 of treatment with the IBET-VHL degrader, MLL-AF9 remained bound to chromatin (**Fig. 5c,**
450 **e and Extended Data Fig. 5b**). Collectively, these data emphasise two important previously
451 unappreciated facts (i) MLL-FP are bound at chromatin in a manner that is insensitive to the
452 transcriptional status of the locus and (ii) that both H3K79me2 and Menin are specifically
453 important for the chromatin occupancy of MLL-FP.

454

455 Whilst loss of H3K79me2 clearly resulted in a displacement of MLL-AF9, we and others have
456 previously demonstrated that despite rapid enzymatic inhibition of DOT1L, H3K79me2 levels
457 require several days to decrease^{7,62}. Therefore, it remained unclear what role H3K79me2 plays
458 in the immediate early transcriptional regulation of MLL-AF9 target genes. Similarly, although
459 Menin inhibition has recently been shown to unexpectedly result in a decrease in H3K79me2
460 levels, the molecular mechanism underpinning this observation is unknown⁶³. To address these
461 questions, we first sought to determine the transcriptional changes that are induced following
462 treatment with SGC0946 and VTP50469 for 72hrs and 24hrs, respectively, on the core MLL-
463 AF9 targets we identified. We chose these time points as this is when we and others observed
464 efficient displacement of MLLAF9 from chromatin with these specific inhibitors of DOT1L

465 and Menin⁵⁶(**Fig. 5b, d**). We found that most of the genes repressed after MLL-AF9
466 degradation were also downregulated by both inhibitors, albeit at later time-points (**Fig. 5f and**
467 **Extended Data Fig. 5c**).

468
469 Although the same genes were regulated by MLL-AF9 degradation, Menin and DOT1L
470 inhibition, our data raised the prospect that the time frame in which these genes were altered
471 with each of these interventions was substantially different. Given the slow turnover of
472 H3K79me2 we considered the possibility that the levels of H3K79me2 alone are insufficient
473 to maintain transcription of MLL-FP targets. To explore this further, we first wanted to
474 determine the kinetics of Menin inhibition in relation to DOT1L inhibition at the same genes.
475 We performed primary transcript-qPCR (nascent qPCR) after a time course with VTP50469
476 treatment for up to 24hrs and found that Menin inhibition resulted in rapid downregulation of
477 key targets (*Meis1, Jmjd1c, Epha7*) as early as 2 hrs, which closely paralleled our findings with
478 MLL-AF9 degradation (**Fig. 5g**). To understand how this is reflected at chromatin, we
479 performed ChIP-seq for H3K79me2 and MLLAF9-FLAG after early and late treatment with
480 VTP50469 and SGC0946. Consistent with our previous studies using SGC0946, H3K79me2
481 was only reduced after 48hrs of treatment with no global changes detected after 6hrs (**Fig. 5h-**
482 **i**). Importantly, ChIP-seq analysis shows eviction of MLL-AF9 after 6 and 48hrs of VTP50469
483 treatment with no global changes in H3K79me2 (**Fig. 5h-i and Extended Data Fig. 5d**). These
484 results suggest that transcription of key MLL-FP target genes can be markedly suppressed
485 without any change in H3K79me2.

486
487 Interestingly, although global H3K79me2 levels are not changed with Menin inhibition at 6
488 hours or 48hrs (**Fig. 5h**), we observed a potent suppression of H3K79me2 after 48 hrs of
489 VTP50469 treatment at key MLL-target genes (**Fig. 5i**), raising the prospect that the Menin-
490 MLL-Fusion complex recruits DOT1L to chromatin to deposit H3K79me2 at a small subset of
491 genes. Notably, when we looked at the genes where VTP50469 treatment results in
492 transcriptional repression, we find that MLL-AF9 displacement is accompanied by a profound
493 loss of H3K79me2 (**Fig. 5j and Extended Data Fig. 5e-f**). However, even though VTP50469
494 results in a global displacement of MLL-AF9 (**Fig. 5b, d**) not all MLL-AF9 bound genes show
495 a loss of H3K79me2 after displacement of the oncoprotein with Menin inhibition (**Fig. 5k and**
496 **Extended Data Fig. 5e-f**). Taken together, these results suggested a multifactorial regulation
497 of H3K79methylation in MLL-FP leukemia which cannot be solely explained by the simple
498 model of aberrant recruitment of DOT1L by MLL-AF9.

499 **MLLT10 regulates H3K79methylation at regions not occupied by MLL-FP**

500 The selective effects of Menin inhibition and MLLAF9 eviction on H3K79methylation
501 alongside the clear requirement for Menin and MLL-AF9 in the maintenance of leukaemia
502 cells survival, sharply contrasted with the negligible effects on leukaemia cell survival after
503 loss of MLLT10, despite there being a profound global loss of H3K79me2 levels.

504
505
506 To explore the mechanistic basis for this observation, we performed spike-in normalised ChIP-
507 seq for H3K79me2 after depletion of DOT1L or MLLT10 with two independent sgRNAs.
508 These data provided orthogonal confirmation that both MLLT10 and DOT1L regulate

509 H3K79me2 levels globally (**Extended Data Fig. 6a**). Notably, when we look specifically at
510 our previously annotated MLL-AF9 target genes (**Fig. 4h**), we find that H3K79me2 levels are
511 higher at these genes compared with Non-MLL-AF9 target genes (**Fig. 6a-b**). More surprising
512 is that the fact that whilst H3K79me2 levels are markedly reduced after DOT1L loss, there are
513 no changes in H3K79me2 levels at the major MLL-AF9 target genes including MEIS1 and
514 HOXA9 following MLLT10 loss (**Fig. 6a-c and Extended Data Fig. 6b-c**). Together these
515 findings raised the intriguing prospect that in MLL-AF9 leukaemia, DOT1L is functionally
516 partitioned into two separate complexes; one that contains the malignant MLL-AF9 oncogene
517 and one that is the native endogenous DOT1L complex containing MLLT10.

518

519 The possibility of two distinct DOT1L complexes within MLL-AF9 leukaemia cells was
520 further supported by the fact that disruption of MLLT10 in the leukaemia cells appeared to
521 increase H3K79me2 levels at known MLL-AF9 target genes (**Fig. 6c**). To explore this further
522 we looked globally to identify genes where H3K79me2 levels were unchanged or increased
523 following MLLT10 depletion. These data clearly identified ~200 genes where H3K79me2
524 levels were elevated rather than depleted following MLLT10 loss (**Fig. 6d**). Remarkably, when
525 we assess the binding of MLL-AF9 across the genome we find that the genes with the greatest
526 chromatin occupancy of MLL-AF9 are the genes where H3K79me2 levels are increased
527 following MLLT10 loss (**Fig. 6e**). In contrast, H3K79me2 levels decrease after MLLT10
528 depletion at the genes with the lowest occupancy of MLL-AF9 (**Fig. 6b, e**). Together these data
529 suggest that loss of MLLT10 results in the disassembly of the native DOT1L complex
530 containing MLLT10, which in turn results in a relative excess of DOT1L that is able to
531 associate with MLL-AF9 and further accentuate H3K79me2 levels at the major target genes of
532 the oncogenic complex. In further support of this contention, is the striking observation that
533 H3K79me2 was selectively increased directly where MLLAF9 is bound but was reduced in the
534 gene body of MLLAF9 target genes following loss of MLLT10 (**Fig. 6f-g and Extended Data**
535 **Fig. 6d**).

536

537 To further strengthen these findings, we sought to demonstrate the existence of biochemically
538 distinct complexes using size exclusion chromatography. Whilst our use of an epitope tag to
539 MLL-AF9 enabled our detailed studies of chromatin binding in mouse cells, there are
540 unfortunately no reliable antibody reagents to detect mouse MLLT10, DOT1L, ENL and
541 MLLT6. However, as many of the paradigms established for MLL leukaemias in mouse cells
542 are conserved in human cells and moreover shared by several of the common MLL-fusions we
543 chose to biochemically characterise cellular extracts from the most commonly used human
544 MLL-leukaemia cell line MV4;11 containing an MLL-AF4 fusion. When analysed by western
545 blot these data showed that although MLLT10 and DOT1L co-elute (fraction 3), DOT1L but
546 not MLLT10 co-elutes with MLL1 (**Extended Data Fig. 6f**). Taken together with the ChIP-
547 seq analyses these findings are consistent with the existence of two distinct DOT1L complexes
548 in MLL-FP leukaemia: (i) an oncogenic DOT1L complex containing the MLL-FP and (ii) a
549 native DOT1L complex containing MLLT10.

550

551 Our earlier data suggested that whilst Menin inhibition has no influence on the regulation of
552 H3K79me2 by the native endogenous DOT1L complex which includes MLLT10, it does

553 dramatically affect DOT1L activity as it displaces the oncogenic DOT1L complex associated
554 with MLL-AF9 from chromatin (**Fig. 5b, j**). Consistent with the fact that there is a reciprocal
555 re-distribution of DOT1L between the oncogenic and endogenous complexes, we find that
556 displacement of chromatin bound MLL-AF9 after Menin inhibition results in an increase in
557 H3K79me2 at genes dependent on the endogenous MLLT10/DOT1L complex (**Fig. 6h-i**).
558 These results further support the fact that DOT1L exists in both a native MLLT10-dependent
559 complex and an MLL-AF9 oncogenic complex, which together cooperate to regulate
560 H3K79methylation at critical MLL-FP target genes. These data also provide a molecular
561 explanation for the differential regulation of H3K79me2 by Menin inhibition at MLL-AF9
562 target genes (**Fig. 5i-k and Extended Data Fig. 5e-f**).

563

564 **Native and oncogenic DOT1L complexes cooperate to regulate MLL-FP target genes.**

565 To demonstrate the potential clinical implications of the partitioning of DOT1L into two
566 functional complexes, we assessed how abolition of the native complex (through MLLT10
567 loss) impacts the transcriptional response of MLLAF9 cells to VTP50469. We treated control
568 or MLLT10 depleted MLLAF9 cells with a low dose of Menin inhibitor (VTP50469 20nM) or
569 DMSO for 48hrs and performed RNA-seq analysis. When we looked at target genes directly
570 bound and regulated by MLLAF9 (including *Meis1*, *Six1*, and *Epha7*), we found that these
571 genes were substantially more downregulated by Menin-inhibition in the MLLT10 depleted
572 cells compared to control cells (**Fig. 7a**). Indeed, the majority of the Menin/MLLAF9 target
573 genes showed a more pronounced downregulation in MLLT10 depleted cells after VTP50469
574 treatment (**Fig. 7b and Extended Data Fig. 7a**). We next explored whether these
575 transcriptional responses would translate to a functional outcome by performing proliferation
576 assays in the MLLT10 depleted vs control cells treated with VTP50469. These data show that
577 whilst cells deficient in MLLT10 have no growth disadvantage in the absence of drug
578 (**Extended Data Fig. 7b**), the resulting absence of a native DOT1L complex, sensitises the
579 cells to Menin inhibitors (**Fig. 7c and Extended Data Fig. 7b**). To provide a mechanistic
580 explanation for this, we looked at H3K79methylation by ChIP-seq and observed that in the
581 absence of the native DOT1L complex (deletion of MLLT10), H3K79me2 levels were
582 markedly more sensitive to treatment with VTP50469 compared to control cells at MLL-FP
583 target genes (**Fig. 7d and Extended Data Fig. 7c**). These results indicate that specific
584 disruption of the native DOT1L complex causes H3K79me2 at MLL-FP targets to be largely
585 maintained by the oncogenic DOT1L complex, which substantially enhances the
586 transcriptional response and sensitivity to Menin inhibition.

587

588 Since there are currently no small molecules available against MLLT10, we instead used
589 DOT1L inhibitors to determine the potential synergy of targeting the Menin-dependent
590 oncogenic DOT1L complex with Menin inhibition alongside inhibitors of the native DOT1L
591 complex. We demonstrate that combination of DOT1L and Menin inhibitors showed strong
592 synergistic efficacy (**Fig. 7e and Extended Data Fig. 7d-e**). Consistent with the greater
593 functional inhibition of MLL-AF9 cells we also noted that the levels of chromatin bound RNA-
594 Pol II at MLL-AF9 target genes were more dramatically reduced in the combination treated
595 cells (**Fig. 7f**). Taken together, these data highlight that both the oncogenic and native DOT1L
596 complexes cooperate in the maintenance of MLL-FP target gene expression and provide the

597 molecular rationale for potential future combination therapy strategies using DOT1L and
598 Menin inhibitors in MLL-FP leukaemia (**Fig. 8**).

599

600 **Discussion**

601

602 Despite being one of the most intensely studied subset of oncoproteins, the molecular
603 mechanisms by which MLL-FP and its cooperating oncogenic cofactors regulate their target
604 genes remain incompletely understood. Our study sought to address this key issue by focussing
605 on the molecular regulation of a histone modification, H3K79me2, which has been a central
606 focus of the oncogenic process mediated by MLL fusion proteins. Identifying the major
607 regulatory proteins required for histone modifications originally involved a candidate approach
608 which was markedly facilitated by yeast genetics coupled to labour-intensive biochemistry⁶⁴.
609 However, these biochemical strategies alone are unable to assign a functional role to complex
610 members or identify independent functional regulators. As the cornerstone method for
611 understanding chromatin biology has been ChIP⁶⁵, we sought to couple ChIP to high-
612 throughput CRISPR screens to enable a strategy for unbiased discovery of chromatin templated
613 processes. Whilst our CRISPR-ChIP approach can be adapted to study any defined chromatin
614 event, as a proof-of-concept, here we have used it to identify all of the major non-redundant
615 regulators of two highly conserved histone modifications, H3K4me3 and H3K79me2. Using
616 this novel method, we showed that each member of the WRAD complex is essential for
617 efficient deposition of H3K4me3 by the COMPASS and COMPASS-like complexes. CRISPR-
618 ChIP further allowed us to reveal the specific COMPASS complex (SET1A/B) that is likely
619 functioning at the EF1a locus and that Pol II is dispensable for the maintenance of H3K4me3
620 genome-wide in human cells. We subsequently used CRISPR-ChIP to identify MLLT10 and
621 DOT1L as key regulators of H3K79me2 genome-wide. Notably, our unique approach also
622 uncovered an unexpected discrepancy between global H3K79me2 levels and leukaemia cell
623 survival. The prevailing paradigm had suggested that H3K79me2 levels and leukemia cell
624 viability were inexorably linked; however, our unbiased screens had illustrated that global
625 levels of H3K79me2 can be profoundly diminished with loss of MLLT10 with a negligible
626 influence on leukaemia cell survival. We reconcile these observations by illustrating that
627 DOT1L exists in two functionally distinct complexes in MLL-FP leukaemia. The native
628 complex includes MLLT10 which facilitates H3K79 methylation at the majority of
629 transcriptionally active genes but has little influence on the maintenance of the malignant state.
630 In contrast, DOT1L also exists in a neomorphic oncogenic complex with the MLL-FP, which
631 is critical for the maintenance of the malignant transcription program and viability of the
632 leukaemia cells.

633

634 Beyond establishing the molecular regulation of H3K79me2 levels in MLL-leukaemia our data
635 also sought to address another contentious and unresolved issue in the field - is H3K79me2
636 necessary for transcription? Using a combination of approaches to accurately map chromatin
637 occupancy of the MLL-AF9 oncogene and the subsequent rapid and selective degradation of
638 the oncogene coupled to nascent transcriptomics we illustrate several key principles. (i)
639 Although MLL-AF9 is bound to several thousand genes, only ~2% of these genes have a
640 discernible immediate and early decrease in transcriptional output following loss of the

641 oncogene. (ii) The process of transcription per se does not influence the chromatin occupancy
642 of MLL-FP, instead, the chromatin occupancy of this oncogenic fusion is selectively dependent
643 on its interaction with Menin. In this regard, a key insight that our data provides relates to the
644 different kinetics of transcriptional regulation between catalytic inhibition of DOT1L and
645 disruption of Menin-MLL1 interaction. While MLLAF9 degradation and Menin inhibition
646 result in rapid transcriptional repression, DOT1L inhibition takes days to alter transcription.
647 The implications of these findings are important as they illustrate that although H3K79me2 is
648 associated with transcriptional activity, it is not sufficient to maintain transcription and
649 H3K79me2 is not the major regulator of MLL-FP target gene expression. Instead, our data
650 suggests that H3K79me2 is likely required to maintain a chromatin state that is permissive for
651 MLL-AF9 recruitment and binding.

652
653 Finally, our data highlighting the existence of native and oncogenic DOT1L complex provides
654 the molecular explanation for the unexplained observation that Menin inhibition unexpectedly
655 results in a delayed decrease in H3K79me2 at MLL-FP target genes. It also explains why
656 inhibition of Menin in MLL-FP leukaemia results in an increase in gene expression and
657 H3K79me2 levels at genes not bound by Menin or MLL-FP. Understanding how perturbation
658 of one chromatin bound complex results in the dynamic flux of key members between sub-
659 stoichiometric complexes leading to differential gene expression is an important emerging
660 theme in chromatin regulation. Moreover, our findings of functionally distinct DOT1L
661 complexes specifies the molecular rationale for observations of synergy between DOT1L and
662 Menin inhibitors⁶⁶. Taken together, they highlight why targeting both the endogenous and
663 oncogenic DOT1L complexes with combination therapies may increase the therapeutic
664 efficacy and clinical outcomes with these novel therapies against MLL-FP driven leukaemia.
665
666

667 **Acknowledgements**

668 We thank the Flow Cytometry facility and Molecular Genomics Core at the Peter MacCallum
669 Cancer Centre and the ARAFlowcore Flow facility at the Australian Centre for Blood Diseases,
670 Monash University. We thank the following funders for fellowship, scholarship and grant
671 support: VCA Mid-Career Research Fellowship (O.G); Cancer Council Victoria Sir Edward
672 Dunlop Research Fellowship, NHMRC Investigator Grant #1196749 and Howard Hughes
673 Medical Institute International Research Scholarship #55008729 (M.A.D); and NHMRC
674 Project Grants #1146192 (O.G), #1085015 / #1106444 (M.A.D) and #1128984 (M.A.D).

675

676 **Author contributions**

677 O.G and M.A.D conceived, designed and supervised the research and wrote the
678 manuscript. O.G, C.C.B, D.N, D.F, K.K, M.B and C.D conducted experiments and/or analysed
679 data. O.G, C.C.B and K.K performed the CRISPR-ChIP screens. E.Y.N.L and L.T led the
680 analysis of the genomic data and CRISPR-ChIP screens, with contribution from Y-C.C.

681

682 **Data and code availability**

683 Sequencing data has been deposited into the sequence read archive, hosted by the National
684 Center for Biotechnology Information. The accession number for the sequencing data reported
685 in this paper is NCBI sequence read archive: GSE192562.

686

687

688 **Materials and Methods**

689

690 **Cell lines**

691 K562, HEK293T, MOLM-13, MV4;11 and drosophila S2 cells were obtained from ATCC.
692 MLL-AF9 leukaemic blasts were generated by magnetic bead selection (Miltenyi Biotec) of c-
693 KIT⁺ cells from whole mouse bone marrow and subsequent retroviral transduction with an
694 MSCV-FLAGx3-MLL-AF9 construct. K562, MV4;11 and MOLM-13 cells were cultured in
695 RPMI-1640 supplemented with 2mM Glutamax, 100 IU/mL Penicillin, 100 µg/mL
696 Streptomycin and 10% HI-FCS. HEK293T cells were cultured in DMEM supplemented with
697 2mM Glutamax, 100 IU/mL Penicillin, 100 µg/mL Streptomycin and 10% HI-FCS. MLL-AF9
698 cells were cultured in RPMI-1640 supplemented with 2 mM Glutamax, 100 IU/mL Penicillin,
699 100 µg/mL Streptomycin, 10% HI-FCS, IL-3 10 ng/mL, IL-6 10 ng/mL and SCF 50 ng/mL
700 (Peprotech) for the first two weeks and then IL-3 10ng/mL for ongoing culturing. Drosophila
701 S2 cells were cultured in Schneider's Drosophila media (Life Technologies) supplemented with
702 100 IU/mL Penicillin, 100 µg/mL Streptomycin and 10% HI-FCS. All cell lines were cultured
703 in 5% CO₂ at 37°C with the exception of Drosophila S2, which was cultured at room
704 temperature. All cell lines were subjected to regular mycoplasma testing and underwent short
705 tandem repeat (STR) profiling.

706

707 **Chemicals**

708 SGC0946 was obtained from structural genome consortium, VTP50469 and A-485 were
709 purchased from Selleck chemicals. For each inhibitor doses used, and durations of treatment
710 are indicated in figure legends. For ChIP-qPCR, A-485 was used at a dose of 3µM for 24hrs.
711 For ChIP-seq experiments, VTP50469 was used at a dose of 500nM and cells typically
712 harvested at 48hrs unless otherwise indicated. SGC0946 was used at a dose of 5µM for 72hrs.
713 DMSO was used as vehicle control for all drug treatment experiments.

714

715 **CRISPR sgRNA library**

716 The targeted sgRNA CRISPR library is a custom built ~7239 human and ~7395 mouse sgRNAs
717 Targeting ~1144 chromatin regulators (6sgRNAs per gene), as well as non-targeting and safe
718 targeting control sgRNAs (guide sequences are provided in Table S1). Library sgRNAs were
719 expressed in the CRISPR-ChIP plasmid, which is a modified pKLV-U6gRNA(BbsI)-
720 EF1a_{purO}2A_{BFP} lentiviral sgRNA expression vector, which encodes puromycin and BFP
721 selection markers obtained from Addgene #50946, a gift from Kosuke Yusa⁶⁷ as described.
722 Murine *Meis1* promoter comprised of ~1.4kb upstream of TSS
723 Murine *Myc* enhancer was obtained from H3K27ac ChIP-seq and ATAC-seq data⁶⁸ and cloned
724 upstream of a minimal CMV promoter. 500bp of human PGK promoter and 1kb of human
725 EF1a promoter including 5'UTR intron. The cis-elements were cloned into the PKLV guide
726 plasmid ~40bp downstream of the guide sequence.

727

728 **CRISPR-ChIP screens**

729 K562 and MLLAF9 cells were transduced with a lentiviral vector encoding Cas9-IRES
730 mCherry. mCherry positive cells were sorted as single cells to obtain a clonal population of
731 high cas9 expressing cells.

732

733 Cas9 cells ($>100 \times 10^6$ per cell line) were infected with the pooled lentiviral sgRNA library at
734 a multiplicity of infection of 0.3. The percentage of cells infected was determined by flow
735 cytometry-based evaluation of BFP⁺ (sgRNA-expressing) cells 48 hours following
736 transduction of the targeted epigenetic library. Infected cells were selected with 2 $\mu\text{g}/\text{mL}$
737 puromycin commencing 48 hours after transduction. Viable cells were collected and sorted at
738 day 6 (Pol II, H3K4me3) and day 9 (H3K79me2) for ChIP as well as library control (input)
739 samples. For the ChIP samples, $\sim 120 \times 10^6$ cells were cross linked with 1% formaldehyde
740 (Sigma-aldrich). For the library control samples $\sim 5\text{-}10 \times 10^6$ cells were harvested for genomic
741 DNA. Lysed cells for ChIP were sonicated to obtain average fragment size of 1-2kb to ensure
742 gRNA remains linked to promoter sequence. ChIP was performed as previously described, with
743 some modifications, $\sim 8\text{-}10 \times 10^6$ cells' worth of chromatin was incubated with 2-4 μg of antibody
744 in separate tubes, between 12-15 ChIP tubes per CRISPR-ChIP experiment was used. 50ul of
745 Protein A or G beads was added to each tube after O/N incubation followed by washing and
746 elution. Elution was performed twice and de-crosslinked O/N. ~ 12 ChIP tubes were purified
747 using Qiagen PCR purification columns. 3 ChIP tubes were purified across one PCR cleanup
748 column and column elution was performed at least 4 times in 50ul volume with heated
749 nuclease-free water to maximise the yield of ChIP DNA.

750

751 One-step PCR was performed to amplify the guide sequence from ChIP DNA or genomic
752 DNA, containing adaptors for Illumina sequencing. Samples were sequenced with single-end
753 75 bp reads on an Illumina NextSeq500. The sequence reads were trimmed to remove the
754 constant portion of the sgRNA sequences with fastx clipper
755 (http://hannonlab.cshl.edu/fastx_toolkit/) or cutadapt v1.14⁶⁹, then mapped to the reference
756 sgRNA library with bowtie2⁷⁰. After filtering to remove multi-aligning reads, the read counts
757 were computed for each sgRNA. MAGECK was used to rank the genes for which targeting
758 sgRNAs were significantly enriched in the ChIP samples compared to the control samples
759 taken from the same pool of growing mutagenized cells. MAGECK analysis of CRISPR-ChIP
760 screens is in the Supplementary Tables 2-3, and CRISPR-dropout analysis is in Supplementary
761 Table 4.

762

763 **CRISPR/Cas9-mediated gene disruption**

764 Single guide RNA (sgRNA) oligonucleotides (Integrated DNA Technologies) were cloned into
765 lentiviral expression vectors pKLV-U6gRNA(BbsI)-PGKpuro_{2A}BFP (Addgene #50946, a gift
766 from Kosuke Yusa)⁶⁷ as described. Oligonucleotide sequences are listed in Table 2, with
767 sources as indicated^{71,72}. For CRISPR/Cas9-mediated gene disruption, cells were first
768 transduced with the Cas9 expression vector pHRSIN-P_{SFFV}-Cas9-P_{PGK}-Blasticidin⁷³ or
769 FUCas9Cherry (a gift from Marco Herold, Addgene #70182)⁷⁴, and selected with blasticidin
770 or sorted for mCherry expression respectively. To generate polyclonal populations with
771 targeted gene disruption, cells were subsequently transduced with pKLV-gRNA-
772 PGKpuro_{2A}BFP encoding either gene-specific sgRNAs or with a control sgRNA targeting a
773 'safe' genomic location with no annotated function⁷¹. Cells infected with pKLV-gRNA-
774 PGKpuro_{2A}BFP were selected with 2 $\mu\text{g}/\text{mL}$ puromycin for 72 hours, commencing 48 hours

775 after transduction. Efficient functional CRISPR/Cas9-mediated gene disruption of target genes
776 was confirmed by immunoblot or sanger sequencing using TIDE analysis.

777

778 **Virus production and transduction**

779 Lentivirus was produced by triple transfection of HEK-293ET cells with a lentiviral transfer
780 vector and the packaging plasmids psPAX2 and pMD.G at a 0.5:0.35:0.15 ratio. Retrovirus
781 was produced by triple transfection of HEK-293ET cells with a retroviral transfer vector,
782 structural pMD1-gag-pol plasmid and pMD.G envelope plasmid at a 0.75:0.22:0.03 ratio. All
783 transfections were performed using polyethylenimine (PEI). Viral supernatants were collected
784 48 hours following transfection, filtered through a 0.45 μm filter and added to target cells.

785

786 **Flow cytometry**

787 Cells were washed in PBS/2% FCS, samples were resuspended in PBS with 2% FCS and
788 filtered. Data were acquired on a BD LSRFortessa or BD FACSymphony and analysed in
789 FlowJo or sorted using a BD FACSFusion sorter.

790

791 **Immunoblotting**

792 Cells were lysed in 1% SDS in 100 mM Tris-HCl pH 8.0 with Roche cOmplete EDTA-free
793 protease inhibitor at room temperature. DNA was fragmented by adding 1:100 Benzonase
794 (Sigma). Lysates were heated to 70°C in SDS sample buffer with 50 mM DTT for 10 minutes,
795 separated by SDS-PAGE and transferred to PVDF membrane (Millipore). Membranes were
796 blocked in 5% milk in TBS-T and incubated with indicated antibodies O/N at 4 degrees. Blots
797 were imaged with ECL prime using a gel doc instrument.

798

799 **Size exclusion chromatography**

800 MV411 cell extract from 50 x 10⁶ cells in 500 μL was clarified by centrifugation at 21,000 g
801 at 4°C for 10 min. 500 μL sample was then injected into a 500 μL loop and was loaded onto a
802 Superose 6 Increase 10/300 GL column (Cytiva) equilibrated with Buffer A (50 mM HEPES
803 pH 7.5, 250 mM NaCl, 10% glycerol, 0.5% Triton X-100, 1 mM DTT, 1 mM EDTA, 1mM
804 AEBSF, 20 μM leupeptin, 1 μM pepstatin, 1 mM PMSF). Fractions of 300 μL were collected
805 at a flow rate of 0.5 mL/min. Fractions were precipitated by the addition of 4 volumes of cold
806 acetone and stored overnight at -80°C. Proteins were pelleted by centrifugation at 21,000 g at
807 4°C for 20 min. Pellets were washed with cold acetone, air dried, resuspended in Laemmli
808 buffer (10% glycerol, 2% SDS, 60 mM Tris-HCl pH 6.8, 0.02% bromophenol blue, 2.5% 2-
809 mercaptoethanol) and were then subjected to SDS-PAGE and immunoblotting.

810 **Antibodies**

811 The following antibodies were used for western blot and/or ChIP analyses: anti-HSP60
812 (sc13966, Santa Cruz Biotechnology), anti-H3K27ac (ab4729, Abcam), anti-H3K4me3
813 (ab8580, Abcam), anti-H3K79me2 (ab3594, Abcam), Anti-H3 total (ab1791, Abcam), anti-
814 SET1A (clone-D3VPS, 61702S, Cell Signalling), anti-MLL1 (D2M7U, 14689S, Cell
815 Signalling), anti-MLL2/KMT2B (D6X2E, 63735S, Cell Signalling), anti-Pol II (CTD4H8, 05-
816 623, Millipore), anti-FLAG M2 antibody (F3165, Sigma). Anti-ENL (ab245520, Abcam), anti-

817 MLLT6 (PA5-30089, ThermoFisher), anti-MLLT10 (PA5-50907, ThermoFisher), anti-
818 DOT1L (ab72454, Abcam) antibodies.

819 qRT-PCR

820 mRNA was prepared with a Qiagen RNeasy kit and cDNA synthesis was performed with a
821 SuperScript VILO kit (Life Technologies), per the manufacturers' instructions. Quantitative
822 PCR analysis was performed on an Applied Biosystems StepOnePlus System or Roche
823 LightCycler 480 Real-Time PCR System with SYBR Green reagents. All samples were
824 assayed in triplicate. Relative expression levels were determined with the ΔC_t method and
825 normalized to *GAPDH*. RT-qPCR primers are listed in Table 1.

826 **Table 1: ChIP-qPCR and Nascent-qRT-PCR primers**

GRNAEF1a (Primer 1) FW	tgaaaaagtggcaccgagtc
GRNAEF1a (Primer 1) RV	Aacttctcggggactgtgg
FW EF1aPURO vector (primer 2) CHIP	tggaatttgccttttgag
RV EF1aPURO vector (primer 2) CHIP	ggcttgactcggtcatggt
FW Neg ctrl 1 ChIP mouse	TGCCATGTGAGTGCAAGAAC
RV Neg ctrl 1 ChIP mouse	ATGGTGGGAGGAAGAAAGGG
Mouse nascent JMJD1c FW	GTCATCCGAGCCGTGTCC
Mouse nascent JMJD1c RV	ccaaacgcaggatggtttt
Mouse nascent Meis1 FW	GAAGTTGAAGTAGGAAGGGAGCC
Mouse nascent Meis1 RV	ggctttaggatcctcattcaa
Mouse nascent EPHA7 FW	CTAAAGAGCTGCGACCCAAC
Mouse nascent EPHA7 RV	tttgcttctctctggcctta
Mouse nascent GAPDH FW	CCCAGCTTAGGTTTCATCAGG
Mouse nascent GAPDH RV	ctcctggcttctgtctttgg
MEIS1 mouse ChIP FW	TCACCACGTTGACAACCTCG
MEIS1 mouse ChIP RV	GCTTCTGCCACTCCAGCTG
EF1a human ChIP FW	Cctgtctcgtgctttcgat
EF1a human ChIP RV	Tggcccgattacaagact
PGK promoter human FW	tgcacacattccacatcca
PGK promoter human RV	tccatttgcacgtcctgca
PGK-Puro FW	cttcaaaagcgcacgtctgc
PGK-Puro RV	ggcttgactcggtcatggt
Meis1-puro FW	TTTCTGCCACTCCAGCTGTC
Meis1-puro RV	ggcttgactcggtcatggt
Myc-mCMV-puro FW	Tggcttgctcagagacacag

827	Myc-mCMV-puro RV	ggcttgactcggtcatggt
828		Aggggcttcagagagtaga
829	FW mouse MYC enhancer	
830		Ggagttgcccttgagatcc
831	RV mouse MYC enhancer	
832		

833

834 **Table 2: sgRNA oligos**

mNT G2 FW	CACCGCTCGTATCTTTTCCACGGC	835
mNT G2 RV	AAACGCCGTGGGAAAAGATACGAGC	836
DOT1L G1 FW	CACCGCTGCAAACATCACTACGGAG	837
DOT1L G1 RV	AAACCTCCGTAGTGATGTTTGCAGC	838
DOT1L G2 FW	CACCGGTCAATGGTGTGCAGATAGT	839
DOT1L G2 RV	AAACACTATCTGCACACCATTGACC	840
MLLT10 G1 FW	CACCGGTTTATTGCGACGGGCA	841
MLLT10 G1 RV	AAACTGCCCGTCGCAATAAACC	842
MLLT10 G2 FW	CACCGAGCTGTGTCCCATAAAGA	843
MLLT10 G2 RV	AAACTCTTTATGGGGACACAGCTC	844
MLLT6 G1 FW	CACCGTTGGCGAACTGCACCTC	845
MLLT6 G1 RV	AAACGAGGTGCAGTTCGCCAAC	846
MLLT6 G2 FW	CACCGCTTGTCGGCATCCGTGG	847
MLLT6 G2 RV	AAACCCACGGATGCCGACAAGC	848
MLLT1/ENL G1 FW	CACCGTCCAGGTGAAGTTAGAGCT	849
MLLT1/ENL G1 RV	AAACAGCTCTAACTTACCTGGAC	850
MLLT1/ENL G2 FW	CACCGCTGGATGTCACACTGCTCA	851
MLLT1/ENL G2 RV	AAACTGAGCAGTGTGACATCCAGC	852
RBBP5 G1 FW	CACCGTGAAGGGAATCGAAACCTC	853
RBBP5 G1 RV	AAACGAGGTTTCGATTCCCTTAC	854
RBBP5 G2 FW	CACCGTGACACTATGTTATCAG	855
RBBP5 G2 RV	AAACCTGATAACATAGTGTCAC	856
ASH2L G1 FW	CACCGCAGGACCAATGTTACTA	857
ASH2L G1 RV	AAACTAGTAACATTGGTCCTGC	858
ASH2L G2 FW	CACCGCAACGTCTGCCATCACAGT	859
ASH2L G2 RV	AAACACTGTGATGGCAGACGTTGC	860

861

862 **Cell proliferation and dose–response assays**

863 For proliferation assays, cells were seeded at a consistent density prior to treatment in triplicate
864 and treated with DMSO, VTP50469 or SGC0946 over the indicated time period. Drug was
865 refreshed at least every three days. Cell number was calculated using the BD FACSverse (BD
866 Biosciences), CytoFLEX (Beckman Coulter) or Muse cell counter.

867

868 **sgRNA competition assays**

869 MLL-AF9 Cas9 cells were transduced with lentivirus expressing a gene specific sgRNA. The
870 percentage of BFP-positive cells was measured between day 2 and day 12 after infection and
871 normalised to the percentage of BFP at day 2.

872

873 **ChIP-sequencing**

874 Chromatin immunoprecipitation was performed as described previously⁵⁰. Briefly, for each
875 ChIP, 20 million cells were crosslinked for 15 mins with 1% formaldehyde. Crosslinked
876 material was sonicated to ~200–1000 bp using the Covaris Ultrasonicator e220. Sonicated
877 material was incubated overnight with each antibody, then incubated for 3 h with Protein A
878 magnetic beads. Beads were washed with low and high salt wash buffers, LiCl buffer and TE,
879 before being eluted and decrosslinked overnight. DNA was purified using Qiagen Minelute
880 columns. All ChIP antibodies were used at ~10ug per IP and are listed under the antibodies
881 section. Sequencing libraries were prepared from eluted DNA using Rubicon ThruPLEX DNA-
882 seq kit. Libraries were size selected between 200–500 bps and sequenced on the NextSeq500
883 using the 75 bp single-end chemistry. Chromatin from S2 cells was spiked-in to ChIP-seq
884 experiments involving treatment with SGC0946 or knockout of DOT1L complex components.
885 The S2 chromatin was added to chromatin from leukaemia cells prior to sonication at
886 approximately 5-10% of the cell numbers used for the sample.

887

888 **ChIP-seq analysis**

889 Reads were aligned to the human genome (GRCh37.73) with BWA-mem⁵¹. Duplicate reads
890 and reads mapping to blacklist regions or the mitochondria were removed. Peak calling was
891 performed with MACS2⁵² with default parameters. Genome-browser images of ChIP–seq data
892 was generated by converting the bam files from BWA to TDF files with igvtools and viewing
893 in IGV⁵³. ChIP–seq coverage across selected genomic regions was calculated with BEDtools⁵⁴.
894 Average profile plots were generated using the NGSplot software⁷⁵.

895

896 **RNA-sequencing**

897 RNA was extracted using the Qiagen RNeasy kit. RNA concentration was quantified using a
898 Qubit Fluorometer (Thermo Fisher Scientific). Libraries were prepared using QuantSeq 3'
899 mRNA-seq Library Prep kit (Lexogen). Libraries were sequenced on the NextSeq500 using
900 75 bp single end chemistry.

901

902 **RNA-sequencing analysis**

903 Bcl2fastq (Illumina) was used to perform sample demultiplexing and to convert BCL files
904 generated from the sequencing instrument into Fastq files. Reads were aligned to the human
905 genome (G1k V37) using HiSAT2⁷⁶ and reads were assigned to genes using htseq-count⁷⁷.

906 Differential expression was calculated using DESeq2⁷⁸. Genes with a false discovery rate
907 corrected for multiple testing using the method of Benjamini and Hochberg below 0.05 and a
908 log fold change greater than 1 were considered significantly differentially expressed.
909 Scatterplots depicting log fold change differences between conditions were generated in R
910 using the ggplot2 package and custom R code.

911

912 **Quantification and statistical analysis**

913 Statistical analysis was carried out using GraphPad Prism 9. Details of statistical analysis
914 performed are provided in the figure legends. Data were reported as mean \pm SD, SEM or
915 independent replicates shown as individual data points, as indicated in the figure legends.
916 Significance was defined as $p < 0.05$.

917

918

919

920

921

922

923

924

925

926

927

928

929

930

931

932

933

934

935

936

937

938

939

940

941

942

943

944

945 **References:**

- 946 1. Park, P.J. ChIP-seq: advantages and challenges of a maturing technology. *Nature*
947 *reviews. Genetics* **10**, 669-680 (2009).
- 948 2. Przybyla, L. & Gilbert, L.A. A new era in functional genomics screens. *Nature Reviews*
949 *Genetics* (2021).
- 950 3. Nelson, J.D., Denisenko, O. & Bomszyk, K. Protocol for the fast chromatin
951 immunoprecipitation (ChIP) method. *Nature Protocols* **1**, 179-185 (2006).
- 952 4. Qin, J.Y. et al. Systematic comparison of constitutive promoters and the doxycycline-
953 inducible promoter. *PLoS One* **5**, e10611 (2010).
- 954 5. Lasko, L.M. et al. Discovery of a selective catalytic p300/CBP inhibitor that targets
955 lineage-specific tumours. *Nature* **550**, 128-132 (2017).
- 956 6. Daigle, S.R. et al. Selective killing of mixed lineage leukemia cells by a potent small-
957 molecule DOT1L inhibitor. *Cancer Cell* **20**, 53-65 (2011).
- 958 7. Gilan, O. et al. Functional interdependence of BRD4 and DOT1L in MLL leukemia.
959 *Nature Structural & Molecular Biology* **23**, 673-681 (2016).
- 960 8. Shilatifard, A. The COMPASS family of histone H3K4 methylases: mechanisms of
961 regulation in development and disease pathogenesis. *Annual review of biochemistry* **81**,
962 65-95 (2012).
- 963 9. Santos-Rosa, H. et al. Active genes are tri-methylated at K4 of histone H3. *Nature* **419**,
964 407-11 (2002).
- 965 10. Soares, L.M. et al. Determinants of Histone H3K4 Methylation Patterns. *Molecular*
966 *Cell* **68**, 773-785.e6 (2017).
- 967 11. Guenther, M.G., Levine, S.S., Boyer, L.A., Jaenisch, R. & Young, R.A. A chromatin
968 landmark and transcription initiation at most promoters in human cells. *Cell* **130**, 77-88
969 (2007).
- 970 12. Sze, C.C. et al. Coordinated regulation of cellular identity-associated H3K4me3 breadth
971 by the COMPASS family. *Science advances* **6**, eaaz4764-eaaz4764 (2020).
- 972 13. Piunti, A. & Shilatifard, A. Epigenetic balance of gene expression by Polycomb and
973 COMPASS families. *Science* **352**, aad9780 (2016).
- 974 14. Ernst, P. & Vakoc, C.R. WRAD: enabler of the SET1-family of H3K4
975 methyltransferases. *Briefings in Functional Genomics* **11**, 217-226 (2012).
- 976 15. Wu, M. et al. Molecular regulation of H3K4 trimethylation by Wdr82, a component of
977 human Set1/COMPASS. *Mol Cell Biol* **28**, 7337-44 (2008).
- 978 16. Lee, J.H. & Skalnik, D.G. Wdr82 is a C-terminal domain-binding protein that recruits
979 the Setd1A Histone H3-Lys4 methyltransferase complex to transcription start sites of
980 transcribed human genes. *Mol Cell Biol* **28**, 609-18 (2008).
- 981 17. Schneider, J. et al. Molecular regulation of histone H3 trimethylation by COMPASS
982 and the regulation of gene expression. *Mol Cell* **19**, 849-56 (2005).
- 983 18. Krogan, N.J. et al. The Paf1 complex is required for histone H3 methylation by
984 COMPASS and Dot1p: linking transcriptional elongation to histone methylation. *Mol*
985 *Cell* **11**, 721-9 (2003).
- 986 19. Howe, F.S., Fischl, H., Murray, S.C. & Mellor, J. Is H3K4me3 instructive for
987 transcription activation? *Bioessays* **39**, 1-12 (2017).
- 988 20. Pérez-Lluch, S. et al. Absence of canonical marks of active chromatin in
989 developmentally regulated genes. *Nature genetics* **47**, 1158-1167 (2015).
- 990 21. Henikoff, S. & Shilatifard, A. Histone modification: cause or cog? *Trends Genet* **27**,
991 389-96 (2011).
- 992 22. Benayoun, B.A. et al. H3K4me3 breadth is linked to cell identity and transcriptional
993 consistency. *Cell* **158**, 673-88 (2014).

- 994 23. Bieberstein, N.I., Carrillo Oesterreich, F., Straube, K. & Neugebauer, K.M. First exon
995 length controls active chromatin signatures and transcription. *Cell Rep* **2**, 62-8 (2012).
- 996 24. Terzi, N., Churchman, L.S., Vasiljeva, L., Weissman, J. & Buratowski, S. H3K4
997 trimethylation by Set1 promotes efficient termination by the Nrd1-Nab3-Sen1 pathway.
998 *Mol Cell Biol* **31**, 3569-83 (2011).
- 999 25. Ng, H.H., Robert, F., Young, R.A. & Struhl, K. Targeted recruitment of Set1 histone
1000 methylase by elongating Pol II provides a localized mark and memory of recent
1001 transcriptional activity. *Mol Cell* **11**, 709-19 (2003).
- 1002 26. Nguyen, A.T., Taranova, O., He, J. & Zhang, Y. DOT1L, the H3K79 methyltransferase,
1003 is required for MLL-AF9-mediated leukemogenesis. *Blood* **117**, 6912-22 (2011).
- 1004 27. Nguyen, A.T. & Zhang, Y. The diverse functions of Dot1 and H3K79 methylation.
1005 *Genes & Development* **25**, 1345-1358 (2011).
- 1006 28. Mohan, M. et al. Linking H3K79 trimethylation to Wnt signaling through a novel Dot1-
1007 containing complex (DotCom). *Genes Dev* **24**, 574-89 (2010).
- 1008 29. Gilan, O. et al. Functional interdependence of BRD4 and DOT1L in MLL leukemia.
1009 *Nat Struct Mol Biol* **23**, 673-81 (2016).
- 1010 30. Lin, C. et al. AFF4, a component of the ELL/P-TEFb elongation complex and a shared
1011 subunit of MLL chimeras, can link transcription elongation to leukemia. *Mol Cell* **37**,
1012 429-37 (2010).
- 1013 31. Daigle, S.R. et al. Selective killing of mixed lineage leukemia cells by a potent small-
1014 molecule DOT1L inhibitor. *Cancer cell* **20**, 53-65 (2011).
- 1015 32. Okada, Y. et al. hDOT1L links histone methylation to leukemogenesis. *Cell* **121**, 167-
1016 78 (2005).
- 1017 33. Zeisig, D.T. et al. The eleven-nineteen-leukemia protein ENL connects nuclear MLL
1018 fusion partners with chromatin. *Oncogene* **24**, 5525-32 (2005).
- 1019 34. Mueller, D. et al. A role for the MLL fusion partner ENL in transcriptional elongation
1020 and chromatin modification. *Blood* **110**, 4445-54 (2007).
- 1021 35. Wang, X., Chen, C.W. & Armstrong, S.A. The role of DOT1L in the maintenance of
1022 leukemia gene expression. *Curr Opin Genet Dev* **36**, 68-72 (2016).
- 1023 36. Briggs, S.D. et al. Gene silencing: trans-histone regulatory pathway in chromatin.
1024 *Nature* **418**, 498 (2002).
- 1025 37. Ng, H.H., Xu, R.M., Zhang, Y. & Struhl, K. Ubiquitination of histone H2B by Rad6 is
1026 required for efficient Dot1-mediated methylation of histone H3 lysine 79. *J Biol Chem*
1027 **277**, 34655-7 (2002).
- 1028 38. Wood, A. et al. Bre1, an E3 ubiquitin ligase required for recruitment and substrate
1029 selection of Rad6 at a promoter. *Mol Cell* **11**, 267-74 (2003).
- 1030 39. Wang, E. et al. Histone H2B ubiquitin ligase RNF20 is required for MLL-rearranged
1031 leukemia. *Proc Natl Acad Sci U S A* **110**, 3901-6 (2013).
- 1032 40. Cao, Q.F. et al. Characterization of the Human Transcription Elongation Factor Rtf1:
1033 Evidence for Nonoverlapping Functions of Rtf1 and the Paf1 Complex. *Mol Cell Biol*
1034 **35**, 3459-70 (2015).
- 1035 41. Vos, S.M., Farnung, L., Linden, A., Urlaub, H. & Cramer, P. Structure of complete Pol
1036 II–DSIF–PAF–SPT6 transcription complex reveals RTF1 allosteric activation. *Nature*
1037 *Structural & Molecular Biology* **27**, 668-677 (2020).
- 1038 42. Diebold, M.L. et al. The structure of an Iws1/Spt6 complex reveals an interaction
1039 domain conserved in TFIIS, Elongin A and Med26. *EMBO J* **29**, 3979-91 (2010).
- 1040 43. Stadelmayer, B. et al. Integrator complex regulates NELF-mediated RNA polymerase
1041 II pause/release and processivity at coding genes. *Nat Commun* **5**, 5531 (2014).
- 1042 44. Zhu, B. et al. The human PAF complex coordinates transcription with events
1043 downstream of RNA synthesis. *Genes Dev* **19**, 1668-73 (2005).

- 1044 45. Vos, S.M., Farnung, L., Urlaub, H. & Cramer, P. Structure of paused transcription
1045 complex Pol II–DSIF–NELF. *Nature* **560**, 601-606 (2018).
- 1046 46. Kamura, T. et al. The Elongin BC complex interacts with the conserved SOCS-box
1047 motif present in members of the SOCS, ras, WD-40 repeat, and ankyrin repeat families.
1048 *Genes & development* **12**, 3872-3881 (1998).
- 1049 47. Pfleiderer, M.M. & Galej, W.P. Structure of the catalytic core of the Integrator
1050 complex. *Mol Cell* **81**, 1246-1259.e8 (2021).
- 1051 48. Elrod, N.D. et al. The Integrator Complex Attenuates Promoter-Proximal Transcription
1052 at Protein-Coding Genes. *Mol Cell* **76**, 738-752.e7 (2019).
- 1053 49. Chen, F.X. et al. PAF1 regulation of promoter-proximal pause release via enhancer
1054 activation. *Science (New York, N.Y.)* **357**, 1294-1298 (2017).
- 1055 50. Chen, S. et al. The PZP Domain of AF10 Senses Unmodified H3K27 to Regulate
1056 DOT1L-Mediated Methylation of H3K79. *Mol Cell* **60**, 319-27 (2015).
- 1057 51. Bernt, K.M. et al. MLL-rearranged leukemia is dependent on aberrant H3K79
1058 methylation by DOT1L. *Cancer Cell* **20**, 66-78 (2011).
- 1059 52. Wan, L. et al. ENL links histone acetylation to oncogenic gene expression in acute
1060 myeloid leukaemia. *Nature* **543**, 265-269 (2017).
- 1061 53. Erb, M.A. et al. Transcription control by the ENL YEATS domain in acute leukaemia.
1062 *Nature* **543**, 270-274 (2017).
- 1063 54. Nabet, B. et al. The dTAG system for immediate and target-specific protein
1064 degradation. *Nat Chem Biol* **14**, 431-441 (2018).
- 1065 55. Natsume, T., Kiyomitsu, T., Saga, Y. & Kanemaki, M.T. Rapid Protein Depletion in
1066 Human Cells by Auxin-Inducible Degron Tagging with Short Homology Donors. *Cell*
1067 *Reports* **15**, 210-218 (2016).
- 1068 56. Olsen, S.N. et al. MLL::AF9 degradation induces rapid changes in transcriptional
1069 elongation and subsequent loss of an active chromatin landscape. *Mol Cell* **82**, 1140-
1070 1155.e11 (2022).
- 1071 57. Zuber, J. et al. An integrated approach to dissecting oncogene addiction implicates a
1072 Myb-coordinated self-renewal program as essential for leukemia maintenance. *Genes*
1073 *Dev* **25**, 1628-40 (2011).
- 1074 58. Dawson, M.A. et al. Inhibition of BET recruitment to chromatin as an effective
1075 treatment for MLL-fusion leukaemia. *Nature* **478**, 529-33 (2011).
- 1076 59. Zuber, J. et al. RNAi screen identifies Brd4 as a therapeutic target in acute myeloid
1077 leukaemia. *Nature* **478**, 524-8 (2011).
- 1078 60. Winter, G.E. et al. BET Bromodomain Proteins Function as Master Transcription
1079 Elongation Factors Independent of CDK9 Recruitment. *Mol Cell* **67**, 5-18.e19 (2017).
- 1080 61. Gilan, O. et al. Selective targeting of BD1 and BD2 of the BET proteins in cancer and
1081 immunoinflammation. *Science* **368**, 387-394 (2020).
- 1082 62. Kuntimaddi, A. et al. Degree of recruitment of DOT1L to MLL-AF9 defines level of
1083 H3K79 Di- and tri-methylation on target genes and transformation potential.
1084 *CellReports* **11**, 808-820 (2015).
- 1085 63. Krivtsov, A.V. et al. A Menin-MLL Inhibitor Induces Specific Chromatin Changes and
1086 Eradicates Disease in Models of MLL-Rearranged Leukemia. *Cancer Cell* **36**, 660-
1087 673.e11 (2019).
- 1088 64. Allis, C.D., Jenuwein, T. & Reinberg, D. *Epigenetics*, x, 502 p. (Cold Spring Harbor
1089 Laboratory Press, Cold Spring Harbor, N.Y., 2007).
- 1090 65. Furey, T.S. ChIP-seq and beyond: new and improved methodologies to detect and
1091 characterize protein-DNA interactions. *Nat Rev Genet* **13**, 840-52 (2012).
- 1092 66. Dafflon, C. et al. Complementary activities of DOT1L and Menin inhibitors in MLL-
1093 rearranged leukemia. *Leukemia* **31**, 1269-1277 (2017).

- 1094 67. Koike-Yusa, H., Li, Y., Tan, E.P., Velasco-Herrera, M.D.C. & Yusa, K. Genome-wide
1095 recessive genetic screening in mammalian cells with a lentiviral CRISPR-guide RNA
1096 library. *Nat. Biotechnol.* **32**, 267-273 (2014).
- 1097 68. Bell, C.C. et al. Targeting enhancer switching overcomes non-genetic drug resistance
1098 in acute myeloid leukaemia. *Nature Communications* **10**, 2723-15 (2019).
- 1099 69. Martin, M. Cutadapt removes adapter sequences from high-throughput sequencing
1100 reads. *EMBnet Journal* **17**, 10-12 (2011).
- 1101 70. Langmead, B. & Salzberg, S.L. Fast gapped-read alignment with Bowtie 2. *Nat.*
1102 *Methods* **9**, 357-359 (2012).
- 1103 71. Morgens, D.W. et al. Genome-scale measurement of off-target activity using Cas9
1104 toxicity in high-throughput screens. *Nat. Commun* **8**, 15178 (2017).
- 1105 72. Wang, T., Wei, J.J., Sabatini, D.M. & Lander, E.S. Genetic screens in human cells using
1106 the CRISPR-Cas9 system. *Science* **343**, 80-4 (2014).
- 1107 73. Burr, M.L. et al. CMTM6 maintains the expression of PD-L1 and regulates anti-tumour
1108 immunity. *Nature* **549**, 101-105 (2017).
- 1109 74. Aubrey, B.J. et al. An Inducible Lentiviral Guide RNA Platform Enables the
1110 Identification of Tumor-Essential Genes and Tumor-Promoting Mutations In Vivo. *Cell*
1111 *Rep.* **10**, 1422-1432 (2015).
- 1112 75. Shen, L., Shao, N., Liu, X. & Nestler, E. ngs.plot: Quick mining and visualization of
1113 next-generation sequencing data by integrating genomic databases. *BMC Genomics* **15**,
1114 284 (2014).
- 1115 76. Kim, D., Paggi, J.M., Park, C., Bennett, C. & Salzberg, S.L. Graph-based genome
1116 alignment and genotyping with HISAT2 and HISAT-genotype. *Nat. Biotechnol.* **37**,
1117 907-915 (2019).
- 1118 77. Anders, S., Pyl, P.T. & Huber, W. HTSeq—a Python framework to work with high-
1119 throughput sequencing data. *Bioinformatics* **31**, 166-169 (2014).
- 1120 78. Love, M.I., Huber, W. & Anders, S. Moderated estimation of fold change and
1121 dispersion for RNA-seq data with DESeq2. *Genome Biol.* **15**, 550 (2014).
- 1122 79. Li, W. et al. MAGeCK enables robust identification of essential genes from genome-
1123 scale CRISPR/Cas9 knockout screens. *Genome Biology* **15**, 554 (2014).

1124

1125

1126 **Figure legends**

1127

1128 **Figure 1: Establishing the CRISPR-ChIP method.**

1129 **A)** Schematic of vector utilised for the screen highlighting the proximity of the gRNA sequence
1130 to the cis-regulatory element of interest driving expression of a fluorescent reporter. **B)**
1131 Schematic of CRISPR-ChIP proof-of-concept experiment with a mix of two independent
1132 DOT1L and two non-silencing guides sampled at day 2 and day 10 followed by ChIP-PCR
1133 NGS at day 10 for H3K79me2. **C)** H3K79me2 CRISPR-ChIP performed in murine MLL-AF9
1134 cells at day 10 post-infection with a pool of two independent DOT1L and two independent
1135 control (non-silencing) guides. Fold-change depletion of DOT1L guides normalised to control
1136 guides in the library control sample (input) at day 2 and day 10 (Top panel). Fold-change
1137 depletion of DOT1L sgRNAs in the H3K79me2 ChIP at day 10 vs day 10 library control (input)
1138 (Bottom panel). Guide representation was assessed by next-generation sequencing (NGS). **D)**
1139 Schematic of the CRISPR-ChIP workflow. Cells are infected with a lentiviral CRISPR library
1140 (MOI <0.3) and cultured for a desired time period, cells were then collected as a library control
1141 or crosslinked for ChIP with antibody of interest. sgRNAs are amplified by PCR from ChIP
1142 DNA or library control (input) DNA and sequenced by NGS. Differential enrichment of
1143 sgRNAs between ChIP and library control is determined using MAGECK⁷⁹. **E)** The CRISPR-
1144 ChIP chromatin library was transduced into Cas9 negative K562 cells. H3K27ac ChIP was
1145 performed, and guide representation was assessed by NGS in two sampled replicates of library
1146 control and two independent ChIP samples. Data shown are correlation plots of library control
1147 Rep1 vs library control Rep2 (R=0.998), H3K27ac (50x10⁶) Rep1 vs H3K27ac (50x10⁶)
1148 Rep2 (R=0.993), and Library control Rep1 vs H3K27ac Rep1 (50x10⁶) (R=0.985). **F)** Guide
1149 library was down sampled *in silico* at different fold representations, 10⁷ = ~1000-fold
1150 representation down to 10000 guides = ~1fold representation. Guide distribution was plotted
1151 for each sampling event, width of the distribution represents the degree of skewing, with a
1152 wider distribution being more skewed. **G)** Schematic of H3K79me2 CRISPR-ChIP of
1153 SGC0946 timecourse treatment in K562 cells infected with a human guide library and mixed
1154 with DMSO treated K562 cells infected with mouse guide library ~ 1:1 ratio. **H)** Guide
1155 enrichment assessed by NGS and the percentage of human guides remaining in library control,
1156 H3K79me2 in the DMSO or SGC0946 treated samples at the indicated time points is shown.
1157 **I)** Western blot analysis of H3K79me2 levels after treatment with SGC0946 at the indicated
1158 timepoints, antibody against tubulin was used as a loading control.

1159

1160

1161 **Figure 2: Characterising the regulation of H3K4me3 using CRISPR-ChIP.**

1162 **A)** CRISPR-ChIP bubble plot showing the genes required for the maintenance of H3K4me3 at
1163 the EF1a promoter in K562 cells. P-values calculated using MAGECK algorithm. **B)**
1164 Schematic of the COMPASS and COMPASS-like complexes highlighting subunits identified
1165 in the CRISPR-ChIP screen, WRAD complex in green and SET1A/B complex specific
1166 subunits in orange. **C)** Western blot analysis of K562 Cas9 cells infected with control guide
1167 (Safe) or two independent guides targeting ASH2L or RBBP5 using antibodies against
1168 H3K4me3, H3K27ac, Total H3 and HSP60 (loading control). **D)** Profile plot of H3K4me3
1169 ChIP-seq in K562 Cas9 cells transduced with control (NT), ASH2L sgRNA or RBBP5 sgRNA.

1170 **E)** ChIP-seq heatmap of H3K4me3 in K562 Cas9 cells infected with control guides or guides
1171 targeting RBBP5, ASH2L. Showing all genes and ranked based on H3K4me3 levels in control
1172 cells. **F)** Western blot analysis of K562 Cas9 cells infected with control guide (Safe) or two
1173 independent guides targeting Rpb1 (largest subunit of RNA Pol II) using antibodies against
1174 Rpb1, H3K4me3, H3K27ac and HSP60 (loading control). **G)** Profile plot of Pol II ChIP-seq in
1175 K562 Cas9 cells transduced with control (NT), Rpb1 sgRNA (G1) or Rpb1 sgRNA (G2). **H)**
1176 ChIP-seq heatmap of RNA-Pol II in K562 Cas9 cells infected with control guides or two
1177 independent guides targeting Rpb1. Showing all genes and ranked based on RNA-Pol II levels
1178 in control cells. **I)** ChIP-seq heatmap of H3K4me3 in K562 Cas9 cells infected with control
1179 guides or two independent guides targeting Rpb1. Showing all genes and ranked based on
1180 H3K4me3 levels in control cells. **J)** ChIP-seq heatmap of H3K27ac in K562 Cas9 cells infected
1181 with control guides or two independent guides targeting Rpb1. Showing all genes and ranked
1182 based on H3K4me3 levels in control cells.

1183

1184 **Figure 3: MLLT10 and global H3K79me2 are dispensable for the survival of MLL-**
1185 **Fusion leukaemia cells**

1186 **A)** Bubble plot showing the genes required for the maintenance of H3K79me2 at the EF1a
1187 promoter in the CRISPR-ChIP vector in murine MLL-AF9 cells. P-values calculated using
1188 MAGECK algorithm. **B)** Scatter plot of gene dependencies in murine MLL-AF9 cells as
1189 assessed from day 14 of the CRISPR-ChIP screen, highlighted members of the DOT1L
1190 complex (DOTCOM) contained in the library, DOT1L, MLLT10 and MLLT6. **C)** Immunoblot
1191 analysis of H3K79me2, Total H3 and HSP60 in MLL-AF9 Cas9 cells transduced with the
1192 indicated sgRNAs. **D)** sgRNA negative selection competition assays in MLL-AF9 Cas9 cells
1193 transduced with either a non-silencing guide (Control) or guides targeting DOT1L, MLLT10,
1194 MLLT6 or ENL. Percentage of sgRNA positive cells remaining over time. Data represents n=3
1195 experiments. Mean +/- sd. **E)** Analysis of DepMap cell line dependencies comparing MLLT10
1196 vs DOT1L gene effect and MLLT1(ENL) vs DOT1L gene effect across wild-type MLL and
1197 MLL-rearranged acute leukaemia cell lines. Cell lines containing MLL rearrangements are
1198 highlighted in orange. **F)** Correlation plot of RNA-seq LFC between the indicated knockouts
1199 (MLLT10 and ENL) for the top 100 downregulated genes vs DOT1L KO cells.

1200

1201 **Figure 4: Selective regulation of transcription by MLL-AF9.**

1202 **A)** Schematic of retroviral transformation of cKit⁺ HSPC with MLL-AF9 containing a c-
1203 terminal 3xFLAG and mAID tag. **B)** Venn diagram of MLL-AF9 FLAG ChIP-seq peaks from
1204 two replicates. **C)** Heatmap of MLL-AF9 FLAG, Menin, and H3K79me2 ChIP-seq in
1205 MLLAF9-F3-mAID cells. **D)** Genome browser snapshot of MLL-AF9, Menin and H3K79me2
1206 at the *Meis1* locus. **E)** Schematic of the auxin-inducible degron system. **F)** Western blot
1207 analysis of MLL-AF9 degradation following an auxin (IAA) treatment timecourse using
1208 antibodies against FLAG and HSP60 (loading control). **G)** Heatmap of MLL-AF9 ChIP-seq in
1209 DMSO or IAA (2hrs) from MLLAF9-F3-mAID cells. **H)** Volcano plot of differentially
1210 expressed genes from nascent RNA-seq (4su-seq) in MLLAF9-F3-mAID cells treated with
1211 DMSO or IAA for 2hrs. Downregulated genes in blue (<LFC -0.4) and key direct target genes
1212 highlighted in red. **I)** Average profile plot of RNA-Pol IIS2ph ChIP-seq at highly expressed
1213 non-MLLAF9 and MLL-AF9 target genes in DMSO and IAA treated cells. **J)** Genome browser

1214 snapshot of the JMJD1c locus for MLL-AF9 and Pol IIser2 ChIP-seq and 4su-seq after 2hrs of
1215 DMSO or IAA treatment.

1216

1217 **Figure 5: Selective regulation of H3K79me2 at target genes by MLL-AF9**

1218 **A)** Schematic of MLLAF9 oncogene with some of the associated cofactors along with their
1219 targeted therapies. **B)** Heatmap of MLLAF9 ChIP-seq after treatment with either DMSO,
1220 SGC0946 (5uM) for 72hrs, or VTP50469 (500nM) for 48hrs. **C)** Heatmap of MLLAF9 ChIP-
1221 seq after treatment with either DMSO, IBET-151 (500nM) for 8hrs, or IBET-VHL (500nM)
1222 for 8hrs. **D)** Average profile plot of MLLAF9 ChIP-seq across all genes after treatment with
1223 either DMSO, VTP50469 (500nM) and SGC0946 (5uM). **E)** Genome browser snapshots of the
1224 *Meis1* locus in MLLAF9-F3-mAID cells treated with DMSO, SGC0946, VTP50469 or IBET-
1225 151 and IBET-VHL. **F)** Heatmap of downregulated genes from 3'RNA-seq in MLLAF9-F3-
1226 mAID cells treated with SGC0946 (72hrs), IAA (24hrs), or VTP50469 (24hrs). **G)** Nascent
1227 qPCR (primary transcript) analysis of VTP50469 timecourse treatment (500nM) vs DMSO in
1228 MLLAF9-F3-mAID cells using primers against *Jmjd1c*, *Meis1*, and *Epha7*, data normalised to
1229 housekeeping gene (*Gapdh*), error bars represent mean \pm SD from 3 biological replicates. **H)**
1230 Heatmap of H3K79me2 ChIP-seq analysis in MLLAF9-F3-mAID cells treated with either
1231 DMSO, SGC0946 (6hrs), SGC0946 (48hrs), VTP50469 (6hrs), and VTP50469 (48hrs). **I)**
1232 Genome browser snapshot of the *Meis1* locus from the H3K79me2 ChIP-seq in (H). **J)** Average
1233 profile plot of H3K79me2 ChIP-seq across the body of genes downregulated after VTP50469
1234 and bound by MLLAF9 in DMSO, SGC0946, or VTP50469 treatment. **K)** Genome browser
1235 snapshot of exemplar VTP50469 target genes with differential changes in H3K79me2 after
1236 VTP50469, *Meis1* (changed) and *Six1* (unchanged).

1237

1238 **Figure 6: DOT1L functions in distinct native and oncogenic complexes in MLL-FP**
1239 **leukaemia.**

1240 **A)** Average profile plot of H3K79me2 levels at MLL-AF9 target genes in MLL-AF9^{FLAG-mAID}
1241 Cas9 cells transduced with either a non-silencing guide (Control) or 2 independent guides
1242 targeting DOT1L (G1 and G2) or MLLT10 (G1 and G2). **B)** Average profile plot of H3K79me2
1243 levels at the top 500 expressed genes not regulated by MLL-AF9 in MLL-AF9^{FLAG-mAID} Cas9
1244 cells transduced with either a non-silencing guide (Control) or 2 independent guides targeting
1245 DOT1L (G1 and G2) or MLLT10 (G1 and G2). **C)** Genome browser snapshots of canonical
1246 MLL-AF9 target gene *Meis1* and the *Efla* locus used in the CRISPR-ChIP plasmid. Tracks
1247 show levels of H3K79me2 and input in MLL-AF9 Cas9 cells transduced with either a non-
1248 silencing guide (Control) or two independent guides targeting DOT1L or MLLT10. **D)**
1249 Correlation plot of H3K79me2 ChIP-seq peak size in non-silencing control vs MLLT10
1250 knockout (average of two independent guides) showing genes with increased H3K79me2 (red)
1251 or decreased (blue). **E)** Hockey stick plot of genes ranked by ^{FLAG}MLL-AF9 occupancy; red
1252 dots represent genes that display increased H3K79me2 following MLLT10 KO vs non-
1253 silencing guides (Control) while blue dots represent genes with decreased H3K79me2
1254 following MLLT10 KO. **F)** Profile plot of H3K79me2 distribution across MLLAF9 peaks \pm
1255 2kb in MLLAF9^{FLAG-mAID} Cas9 cells transduced with control guides or guides targeting DOT1L
1256 or MLLT10. Red box over the MLL-AF9 peak. **G)** Genome browser snapshot of exemplar
1257 direct and strongly bound MLL-AF9 target gene that shows increased H3K79me2 following

1258 MLLT10 KO in MLL-AF9 cells, *Runx2*. Red box over the MLL-AF9 peak. **H)** Correlation
1259 plot of H3K79me2 normalised count coverage in vehicle treated (DMSO) or Menin inhibitor
1260 (VTP50469) murine MLL-AF9 cells. Genes with a decrease in H3K79me2 following
1261 VTP50469 are highlighted in red and genes with increased H3K79me2 are in blue. **I)** Genome
1262 browser snapshot of an exemplar Menin inhibitor non-responsive gene, *Mxil*, with no MLL-
1263 AF9 occupancy, showing increased H3K79me2 after VTP50469 treatment and decreased
1264 H3K79me2 in MLLT10 KO cells compared to control cells.

1265

1266 **Figure 7: Disruption of the native DOT1L complex sensitises MLLAF9 leukaemia cells**
1267 **to Menin inhibition.**

1268 **A)** Violin plot of RNA-seq in MLLAF9^{FLAG-mAID} Cas9 cells expressing control guides or
1269 MLLT10 guides (stable knockout of MLLT10) and treated with either DMSO or VTP50469
1270 (20nM). Menin inhibitor target genes that are also bound by MLLAF9 are shown. **B)** Lollipop
1271 plot of RNA-seq logFC of the ratio of Control vs MLLT10 KO after treatment with VTP50469
1272 (20nM) in MLLAF9^{FLAG-mAID} cells. **C)** Proliferation assay in control and MLLT10 KO
1273 MLLAF9^{FLAG-mAID} Cas9 cells treated with either DMSO, 20nM or 40nM VTP50469. Cell
1274 counts shown at day 3 and day 7 and normalised to day 1 counts. n=3 biological replicates. *
1275 p <0.05 ** p<0.01. **D)** Genome browser snapshot of exemplar MLLAF9 targets *Meis1* and
1276 *Runx2* from H3K79me2 ChIP-seq in MLLAF9^{FLAG-mAID} cells with control guides or MLLT10
1277 KO and treated with vehicle (DMSO) or VTP50469 (20nM) for 48hrs. MLLAF9 tracks shown
1278 for reference. **E)** Proliferation assay in MLLAF9^{FLAG-mAID} Cas9 cells treated with either
1279 DMSO, SGC0946 (2uM), VTP50469 (10nM, 20nM or 50nM) and combinations. Cell counts
1280 shown at day 4 and day 6 and normalised to day 1 counts. n=3 biological replicates. * p <0.05.
1281 **F)** Profile plot of RNA-Pol II ChIP-seq enrichment at MLLAF9 target genes after treatment
1282 with either DMSO, SGC0946, VTP50469 or Combo for 48hrs.

1283

1284

1285 **Figure 8: Schematic to illustrate the distinct function of the native and oncogenic DOT1L**
1286 **complex.**

1287

1288

1289

1290

1291

1292

1293

1294

1295

1296

1297

1298

1299

1300

1301

1302 **Supplementary figure legends**

1303

1304 **Extended Data Figure 1: A)** ChIP-qPCR analysis of H3K27ac ChIP performed in parental
1305 K562 cells or K562 cells infected with the CRISPR-ChIP plasmid containing an EF1a
1306 promoter. Primers for a negative control region (Neg Ctrl), endogenous EF1a or regions
1307 spanning the gRNA/EF1a (Primer 1), and EF1a/Puro (Primer 2) within the lentiviral CRISPR-
1308 ChIP vector were used, data represents mean +/- SD from two independent biological
1309 replicates. **B)** ChIP-qPCR analysis of H3K27ac, H3K4me3, H3K9ac and RNA-Pol II ChIP at
1310 the endogenous PGK promoter or integrated PGK promoter-Puro reporter, an intergenic region
1311 not enriched in active histone marks was used as a negative control (Neg control). Data
1312 represents mean +/- SD from two independent biological replicates. **C)** ChIP-qPCR analysis of
1313 H3K27ac, H3K4me3, H3K79me2 and RNA-Pol II ChIP at the endogenous Meis1 promoter or
1314 integrated Meis1 promoter (~1.2Kb upstream of TSS)-Puro reporter, an intergenic region not
1315 enriched in active histone marks was used as a negative control (Neg control). Data represents
1316 mean +/- SD from two independent biological replicates. **D)** ChIP-qPCR analysis of H3K27ac,
1317 H3K4me3, and H3K9ac ChIP at the endogenous Myc enhancer or integrated Myc enhancer-
1318 mCMV-Puro sequence, an intergenic region not enriched in active histone marks was used as
1319 a negative control (Neg control). Data represents mean +/- SD from two independent biological
1320 replicates. **E)** ChIP-qPCR analysis of H3K79me2 in K562 cells infected with the CRISPR-
1321 ChIP plasmid and treated with DOT1L inhibitor (SGC0946) for 9 days. Primers for Negative
1322 control region (Neg Ctrl), Meis1, EF1a, and a region spanning the gRNA/EF1a were used, data
1323 represents mean +/- SD from two independent biological replicates. **F)** qPCR analysis of
1324 H3K27ac ChIP in K562 cells infected with the CRISPR-ChIP vector and treated with either
1325 DMSO or CBP/P300 inhibitor (A-485) for 24hrs. Primers for Negative control region (Neg
1326 Ctrl), Meis1, EF1a, and a region spanning the gRNA/EF1a were used, data represents mean
1327 +/- SD from two independent biological replicates. **G)** NGS representation of control guides
1328 (NT) at day 2, day 10, ChIP input day 10, and H3K79me2 ChIP (Left panel). NGS
1329 representation of DOT1L guides at day 2, day 10, ChIP input day 10, and H3K79me2 ChIP
1330 (Right panel).

1331

1332 **Extended Data Figure 2: A)** Correlation plot of library guide counts between H3K27ac ChIP
1333 and a library control sample taken from Cas9 negative K562 cells. H3K27ac ChIP was
1334 performed from different starting cell number, 5 million, 10 million, 25 million, 50 million and
1335 100 million cells. **B)** Bubble plot of H3K27ac ChIP (50M cells) from Cas9 negative K562 cells
1336 analysed using MAGECK. **C)** Correlation plot of RBBP5 KO H3K4me3 LFC vs ASH2L KO
1337 H3K4me3 LFC. **D)** Correlation plot of normalised Pol II levels (rpm) vs normalised H3K4me3
1338 levels (rpm).

1339

1340 **Extended Data Figure 3: A)** Schematic of DOTCOM complex (DOT1L, ENL/MLLT1,
1341 MLLT6/AF17, MLLT10). **B)** Guide counts over time from CRISPR dropout screen in MLL-
1342 AF9 cells for 2 MLLT10 and 2 DOT1L guides. **C)** PCA analysis of RNA-seq from MLLAF9
1343 Cas9 cells transduced with control (non-targeting), DOT1L G1, two independent ENL guides,
1344 two independent MLLT10 guides and two independent MLLT6 guides. **D)** Heatmap of RNA-
1345 seq data described above, showing downregulated genes in the various knockouts as indicated.

1346 **E)** Correlation plot of RNA-seq LFC between two independent MLLT6 sgRNAs and DOT1L
1347 KO for the top 100 downregulated genes in the DOT1L KO cells.

1348

1349 **Extended Data Figure 4: A)** Kaplan-meir curve of mice transplanted with MLLAF9^{FLAG-mAID}
1350 cells or Nras + MLLAF9^{FLAG-mAID}. **B)** Genome browser snapshot of MLLAF9 ChIP-seq
1351 replicates at the meis1 locus. FLAG ChIP from non-FLAG tagged MLLAF9 cells used as a
1352 negative control and input shown. **C)** Genome browser snapshot of MLLAF9 ChIP-seq
1353 replicates at the HOXA cluster. FLAG ChIP from non-FLAG tagged MLLAF9 cells used as a
1354 negative control and input shown. **D)** Proliferation assay of MLLAF9^{FLAG-mAID} Tir1 cells
1355 treated with DMSO or IAA (500uM) over 7 days. **E)** FACS analysis of cell surface Gr1 levels
1356 in unstained, stained, DMSO or IAA treated MLLAF9^{FLAG-mAID} Tir1 cells for 4 days. **F)** Profile
1357 plot of MLLAF9 FLAG ChIP-seq in MLLAF9^{FLAG-mAID} cells treated with DMSO, IAA (2hrs
1358 and 4hrs). **G)** Heatmap of 4su-seq (nascent RNA-seq) in MLLAF9^{FLAG-mAID} Tir1 cells treated
1359 with DMSO or IAA for 2hrs, showing the 260 downregulated genes. **H)** PCA plot of RNA-seq
1360 from MLLAF9^{FLAG-mAID} Tir1 cells treated with DMSO or IAA (2hrs). **I)** Heatmap of RNA Pol
1361 II ser2 ChIP-seq at all genes in MLLAF9^{FLAG-mAID} Tir1 cells treated with DMSO or IAA (2hrs).
1362 **J)** Genome browser snapshots of MLLAF9 targets, *Epha7* and *Baz2b* showing RNA Pol II-
1363 ser2 and MLLAF9 ChIP-seq tracks after treatment with either DMSO or IAA (2hrs).

1364

1365 **Extended Data Figure 5: A)** Heatmap of Menin ChIP-seq in MLLAF9 cells treated with
1366 DMSO, SGC0946 (72hrs) or VTP50469 (48hrs) at all genes. **B)** MLLAF9 FLAG ChIP-seq in
1367 MLLAF9 cells treated with DMSO, IBET151 or IBET-VHL for 8hrs at all genes. **C)** PCA
1368 analysis of RNA-seq data in MLLAF9 cells treated with DMSO, SGC0946 (72hrs), IAA
1369 (24hrs), VTP50469 (24hrs). **D)** Profile plot of MLLAF9 ChIP-seq in MLLAF9 cells treated
1370 with either DMSO, VTP50469 (6hrs), SGC0946 (48hrs) or VTP50469 (48hrs). **E)** Heatmap of
1371 MLLAF9 and H3K79me2 ChIP-seq data in MLLAF9 cells after treatment with VTIP50469
1372 for 48hrs at genes that show decreased H3K79me2 after VTP50469 treatment. **F)** Genome
1373 browser snapshot of ChIP-seq tracks at canonical MLLAF9 target genes, *Jmjd1c* and *Runx2*,
1374 showing MLL-AF9 and H3K79me2 after treatment with VTP50469 or SGC0946 for 48hrs.

1375

1376 **Extended Data Figure 6: A)** Average profile plot of H3K79me2 and input at all genes in
1377 MLL-AF9 cells infected with non-silencing guides (Control), 2 independent DOT1L guides
1378 and 2 independent MLLT10 guides. **B)** Heatmap of H3K79me2 at MLL-AF9 bound genes for
1379 the indicated samples. Genes are ranked from highest to lowest coverage for H3K79me2 in the
1380 control cells. **C)** Genome browser snapshot of a canonical MLLAF9 target, *Hoxa9*, from
1381 H3K79me2 ChIP-seq in MLLAF9 cells transduced with control sgRNA or two independent
1382 guides targeting MLLT10 or DOT1L. **D)** Profile plot of H3K79me2 distribution across
1383 MLLAF9 peaks +/- 10kb in MLLAF9^{FLAG-mAID} Cas9 cells transduced with control guides or
1384 guides targeting DOT1L or MLLT10. **E)** Genome browser snapshots of exemplar direct and
1385 strongly bound MLL-AF9 target genes that show increased H3K79me2 following MLLT10
1386 KO in MLL-AF9 cells, *Jmjd1c* and *Epha7*. **F)** Immunoblot analysis of gel filtration fractions
1387 (superose 6 column) from nuclear extracts of MV4;11 cells (human MLL-AF4) using
1388 antibodies against DOT1L, MLLT10, MLL1, ENL and MLLT6.

1389

1390 **Extended Data Figure 7: A)** Heatmap of RNA-seq data from MLLAF9 Cas9 cells infected
1391 with control or MLLT10 guides and treated with either DMSO or VTP50469 with 20 or 40nM.
1392 **B)** Proliferation assays using MLL-AF9 Cas9 cells transduced with either a control non-
1393 targeting guide or two independent guides targeting MLLT10 (G1 and G2). Cells were treated
1394 with either DMSO, VTP50469 25nM or 50nM. Plots represent n=3 biological replicates. Bars
1395 represent mean +/- SD **C)** Profile plot of H3K79me2 ChIP-seq in MLLAF9 Cas9 cells infected
1396 with control or MLLT10 guides and treated with DMSO or VTP50469 (20nM) for 48hrs.
1397 Analysis performed across MLLAF9 target genes. **D)** Proliferation assay in MOLM13 cells
1398 treated with either DMSO, SGC0946 (3uM), VTP50469 (100nM) or combination. Mean +/-
1399 SD from n=3 biological replicates. **E)** Proliferation assay in MLLAF9^{FLAG-mAID} Cas9 cells
1400 treated with either DMSO, SGC0946 (3uM), VTP50469 (50nM) or combination. Cell counts
1401 shown at day 4 and day 6 and normalised to day 1 counts. Mean +/- SD from n=3 biological
1402 replicates. * p <0.05.

1403
1404
1405
1406
1407
1408
1409
1410
1411
1412
1413
1414
1415
1416
1417
1418
1419
1420
1421
1422

Figure 1

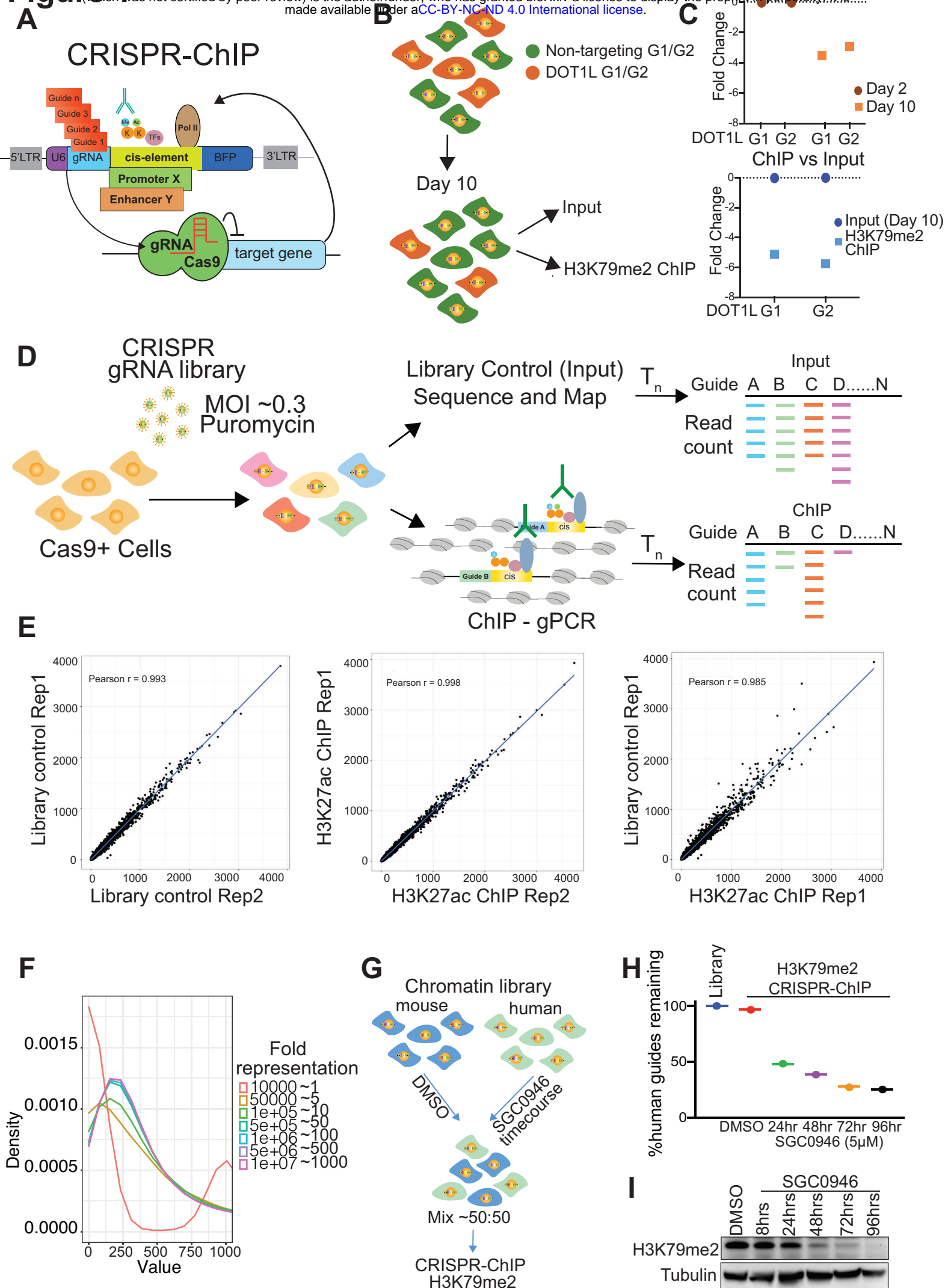


Figure 2

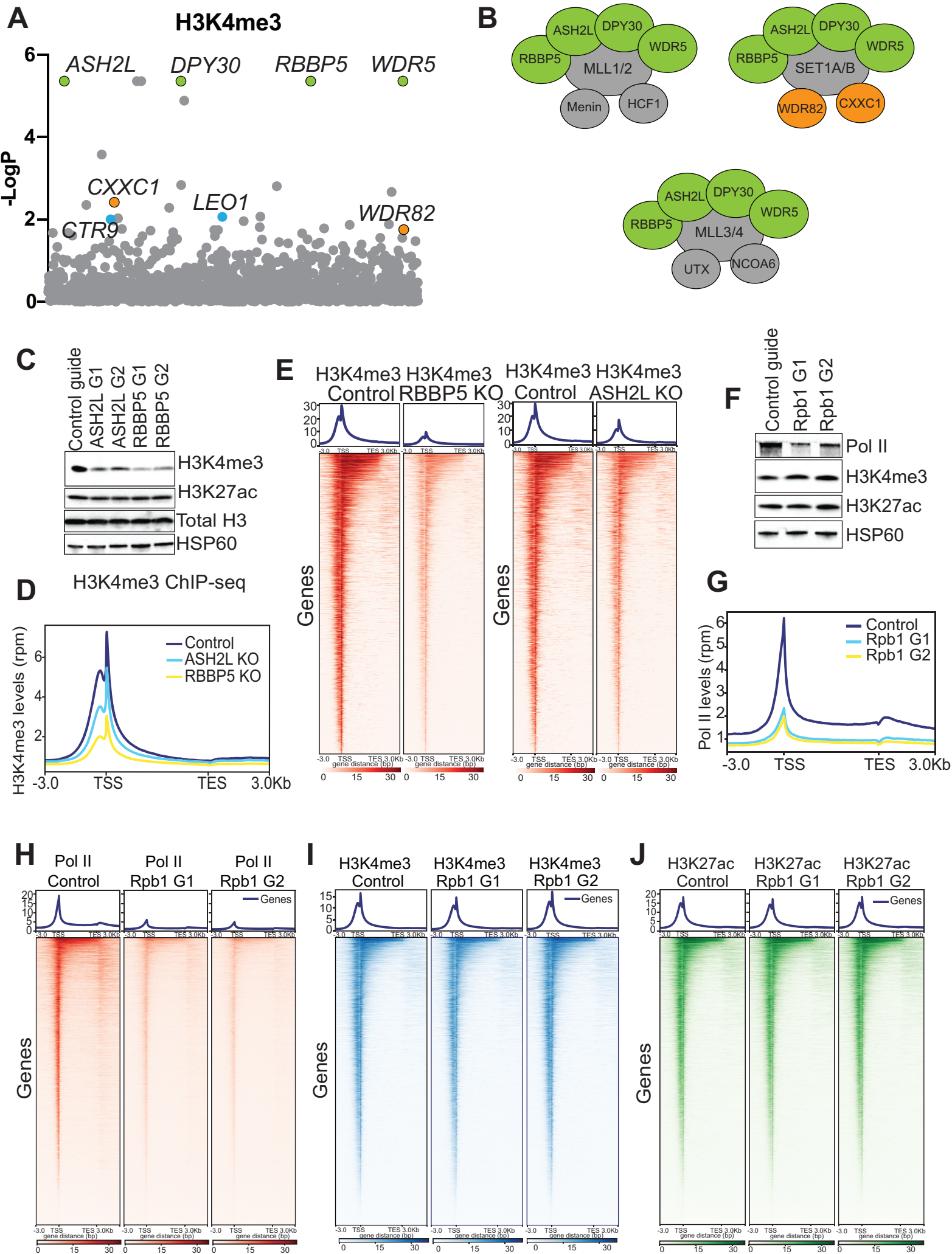


Figure 3

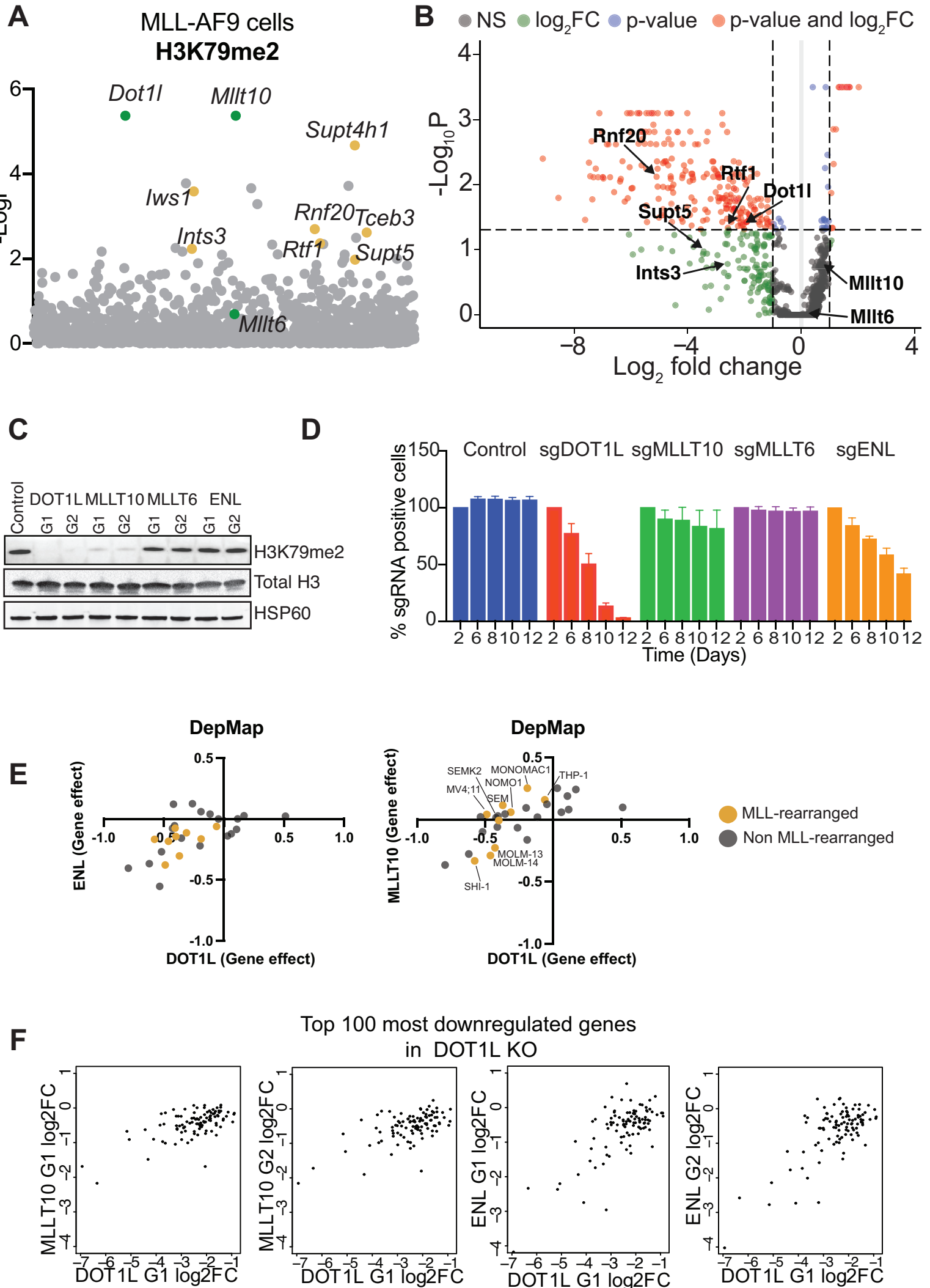


Figure 4

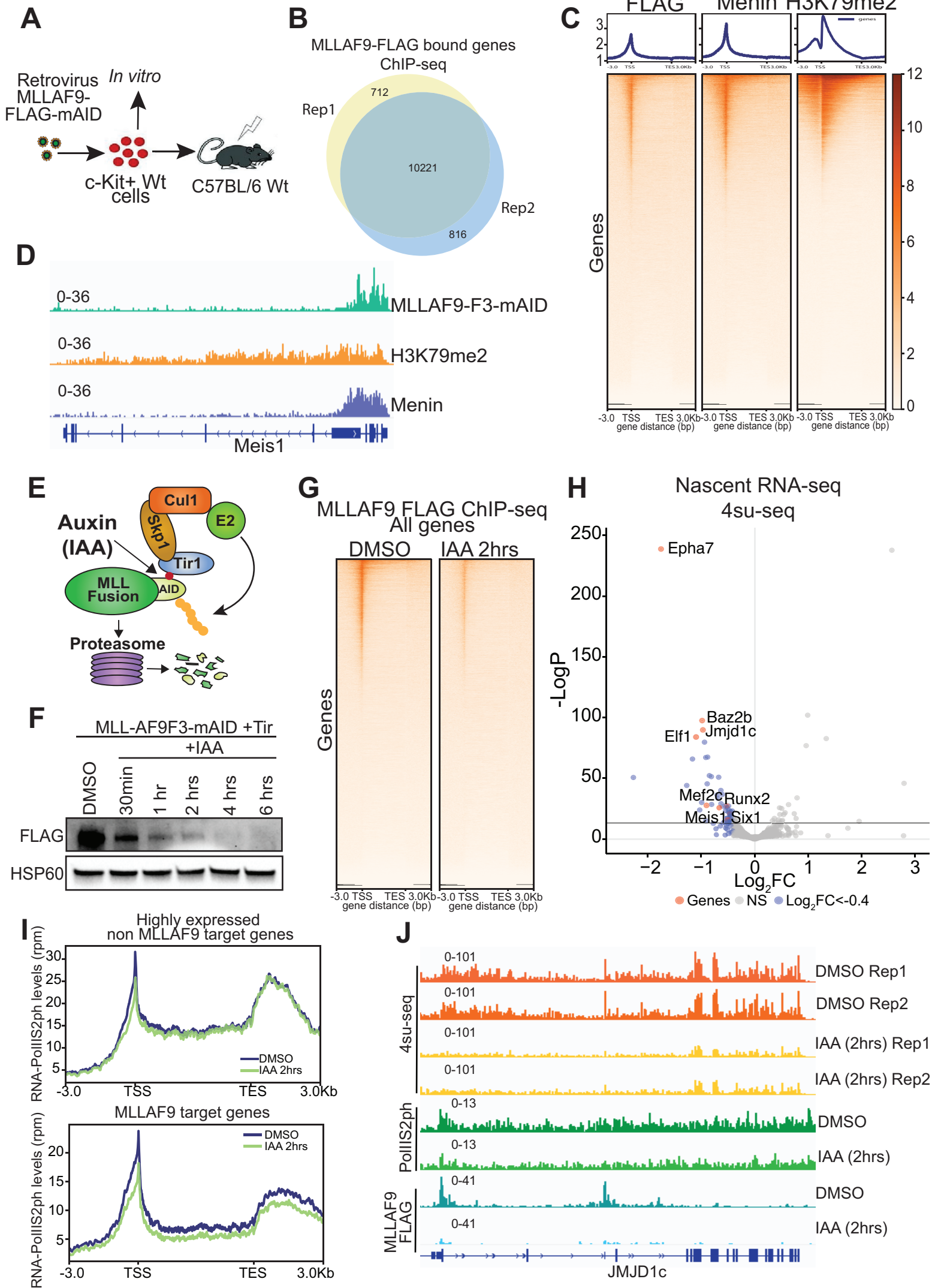


Figure 5

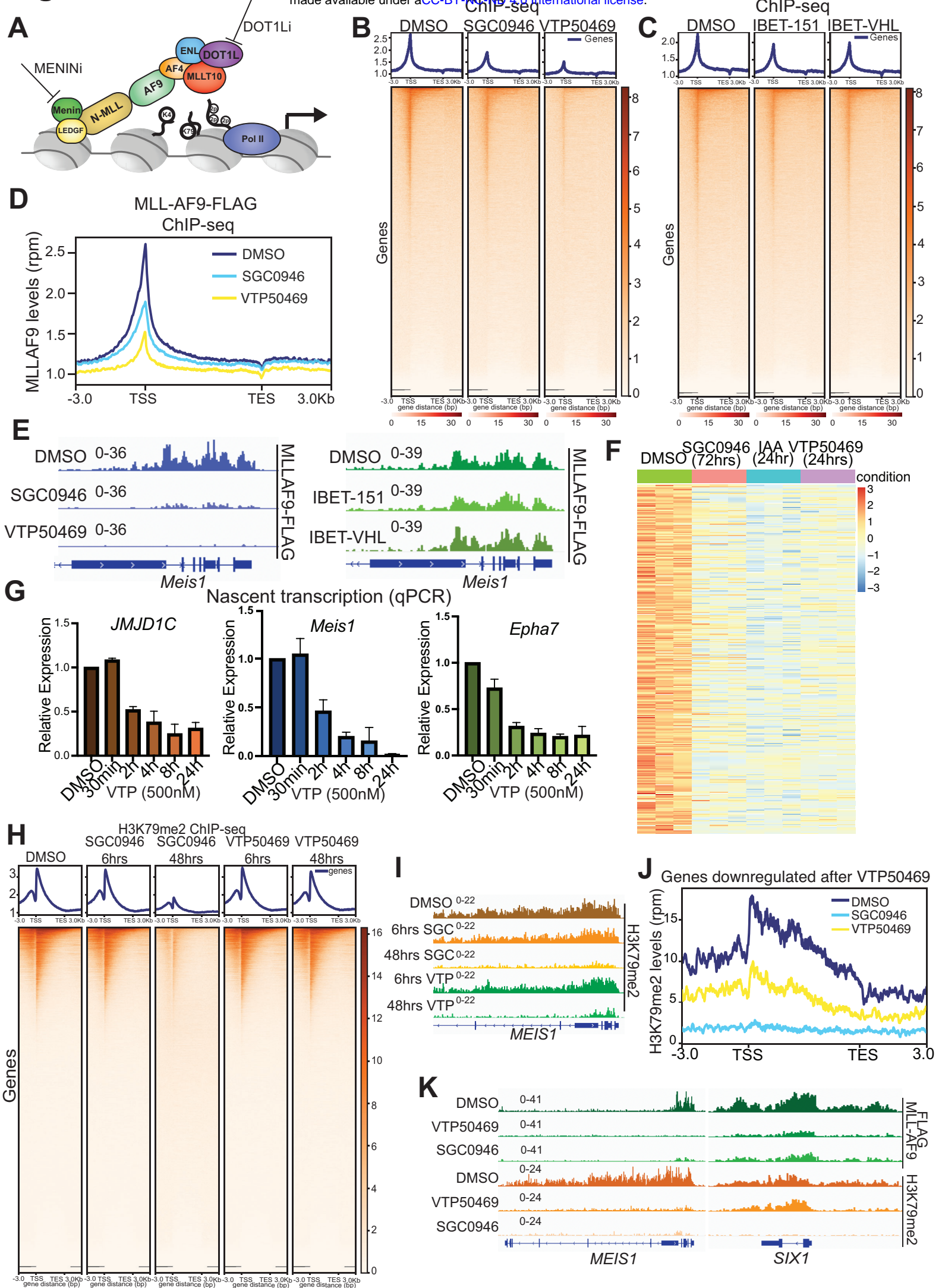
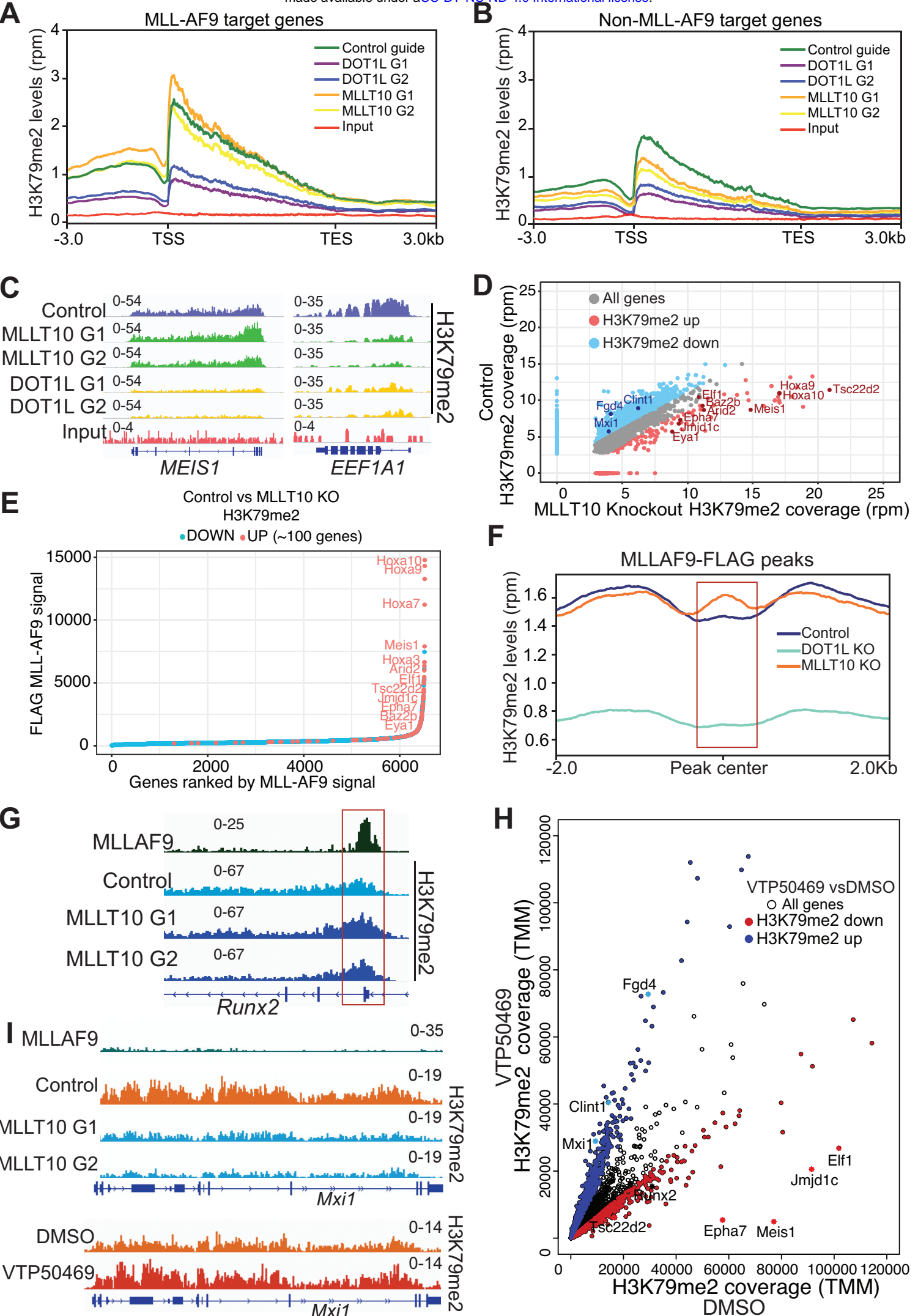
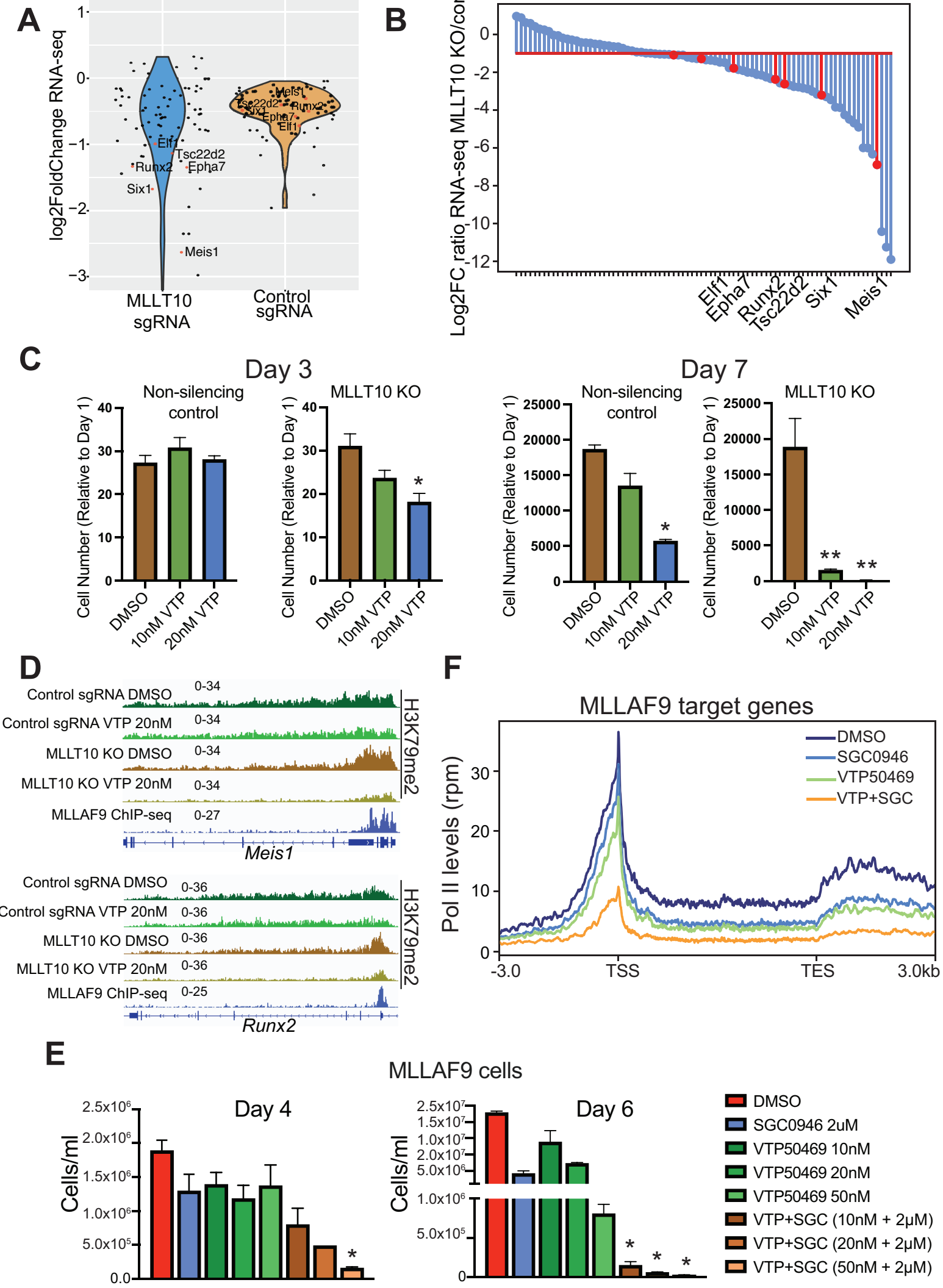
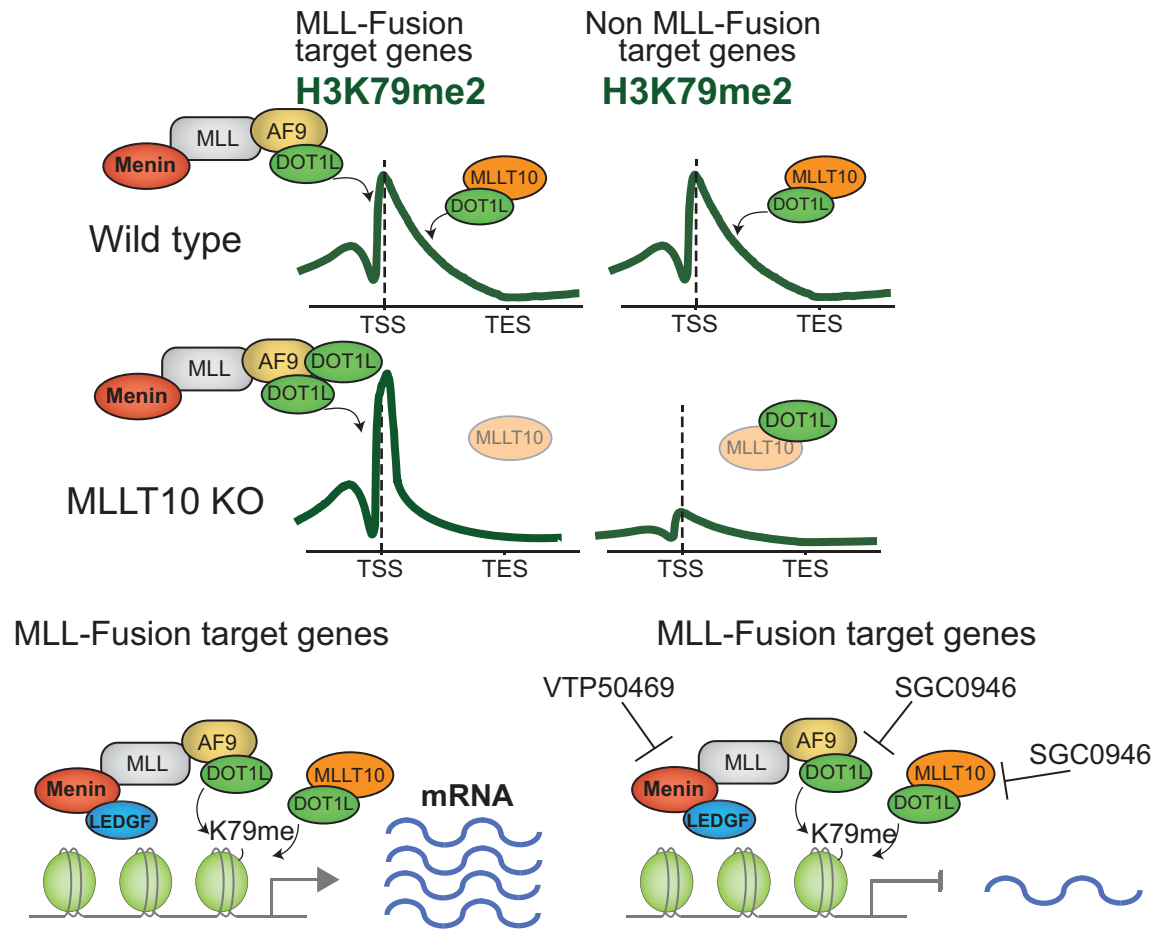


Figure 6

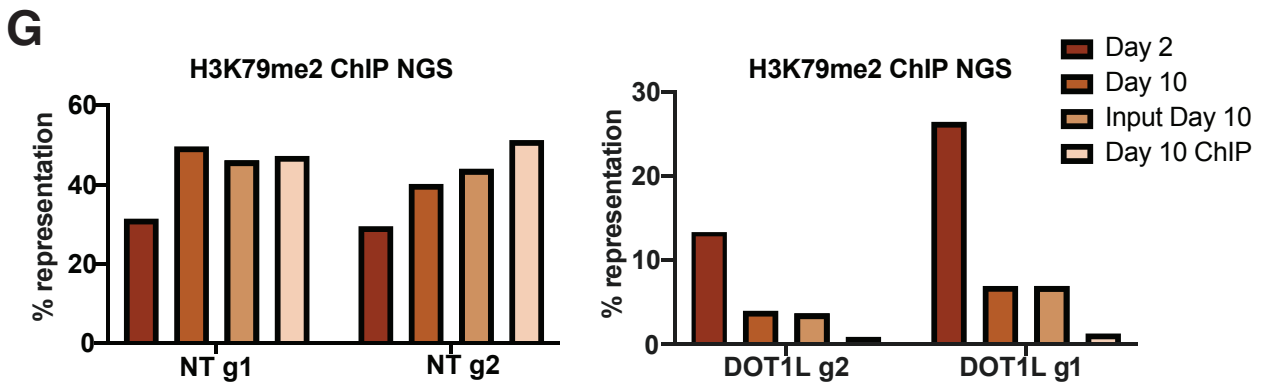
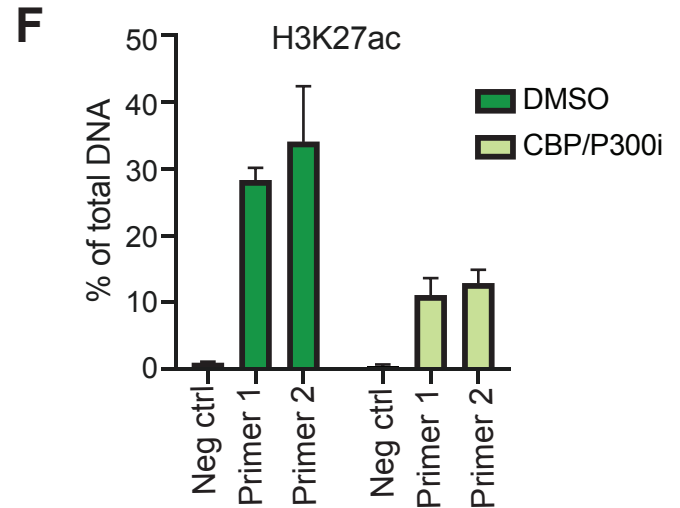
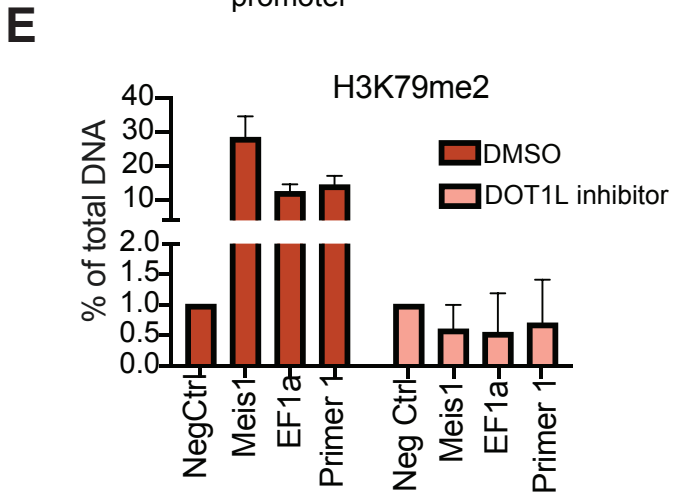
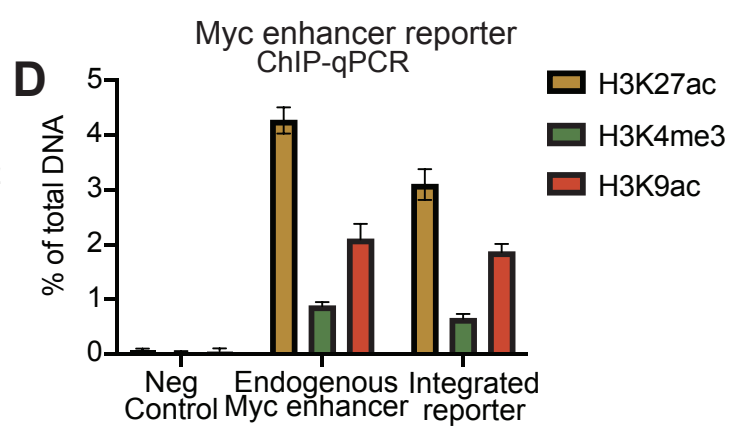
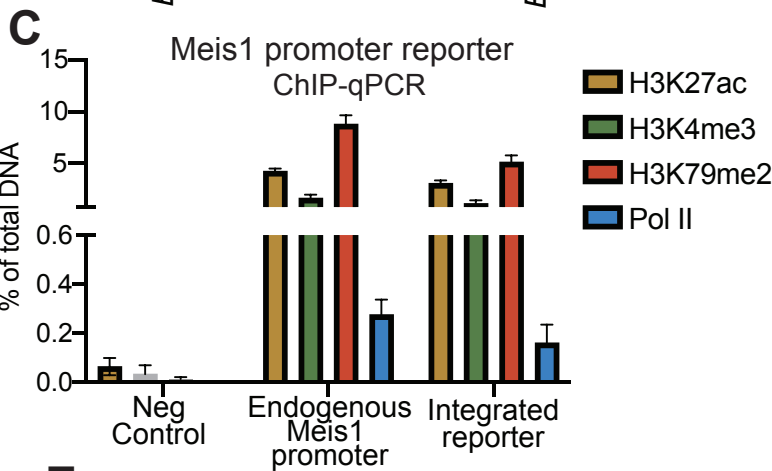
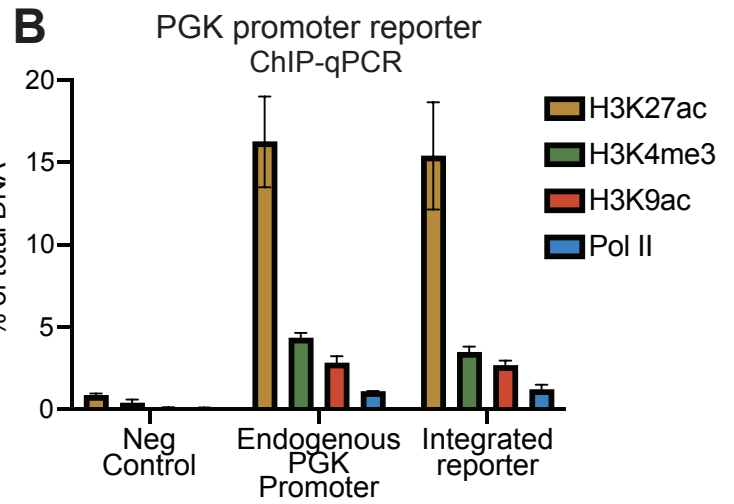
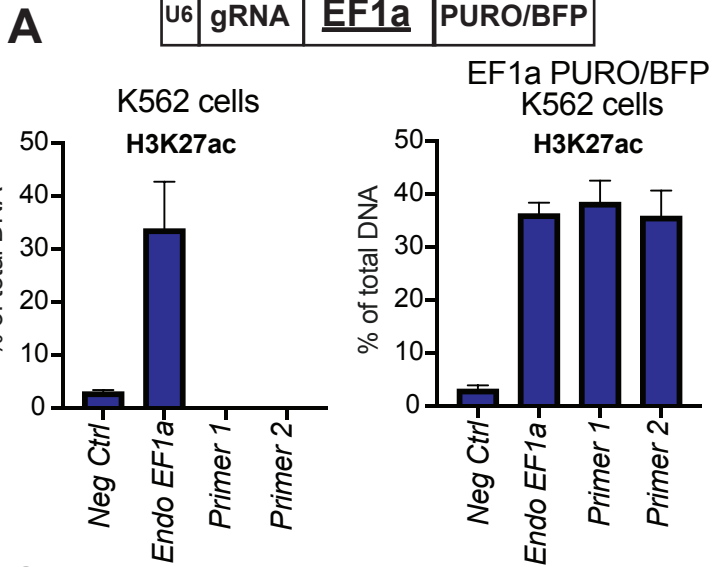


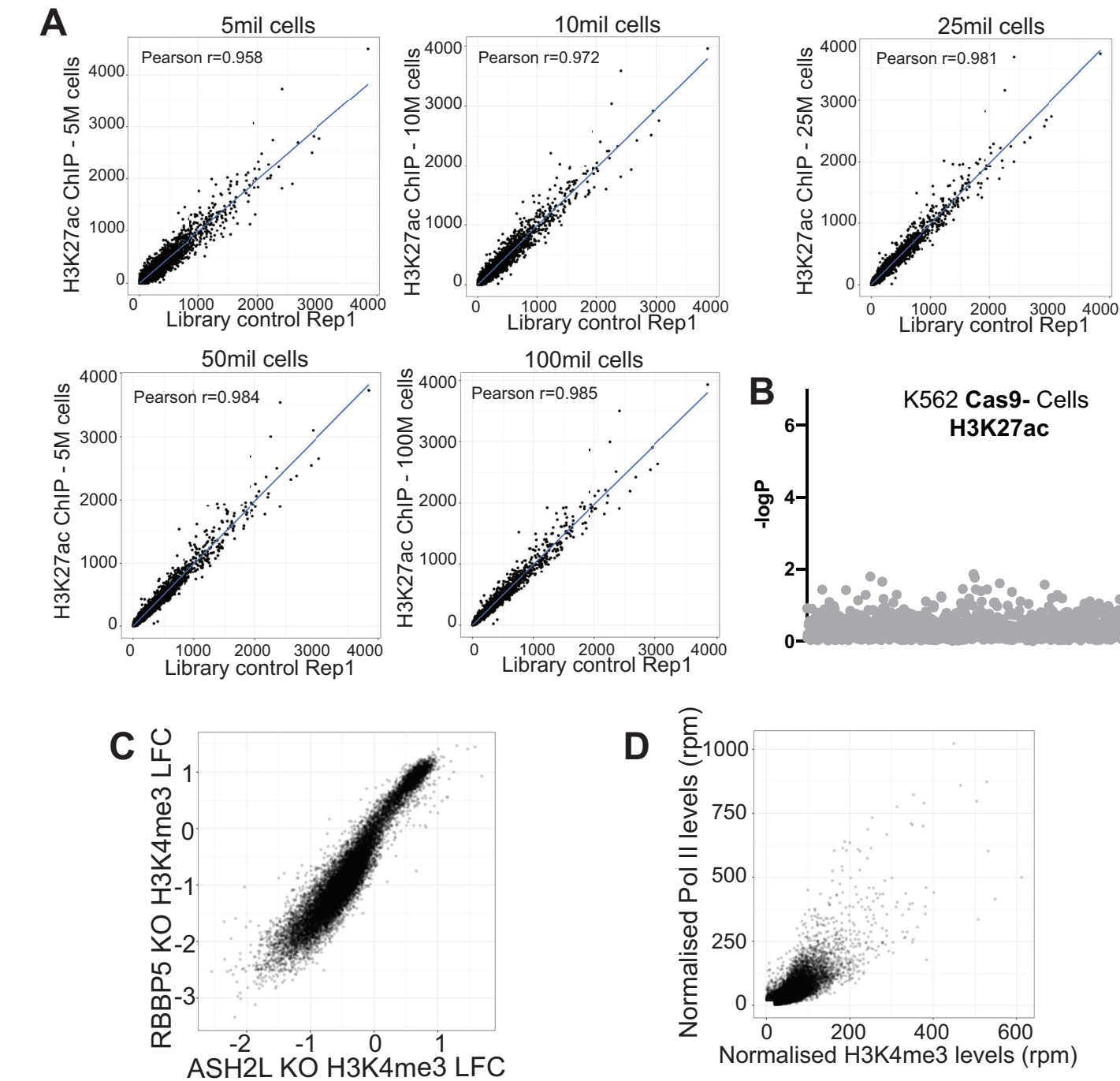




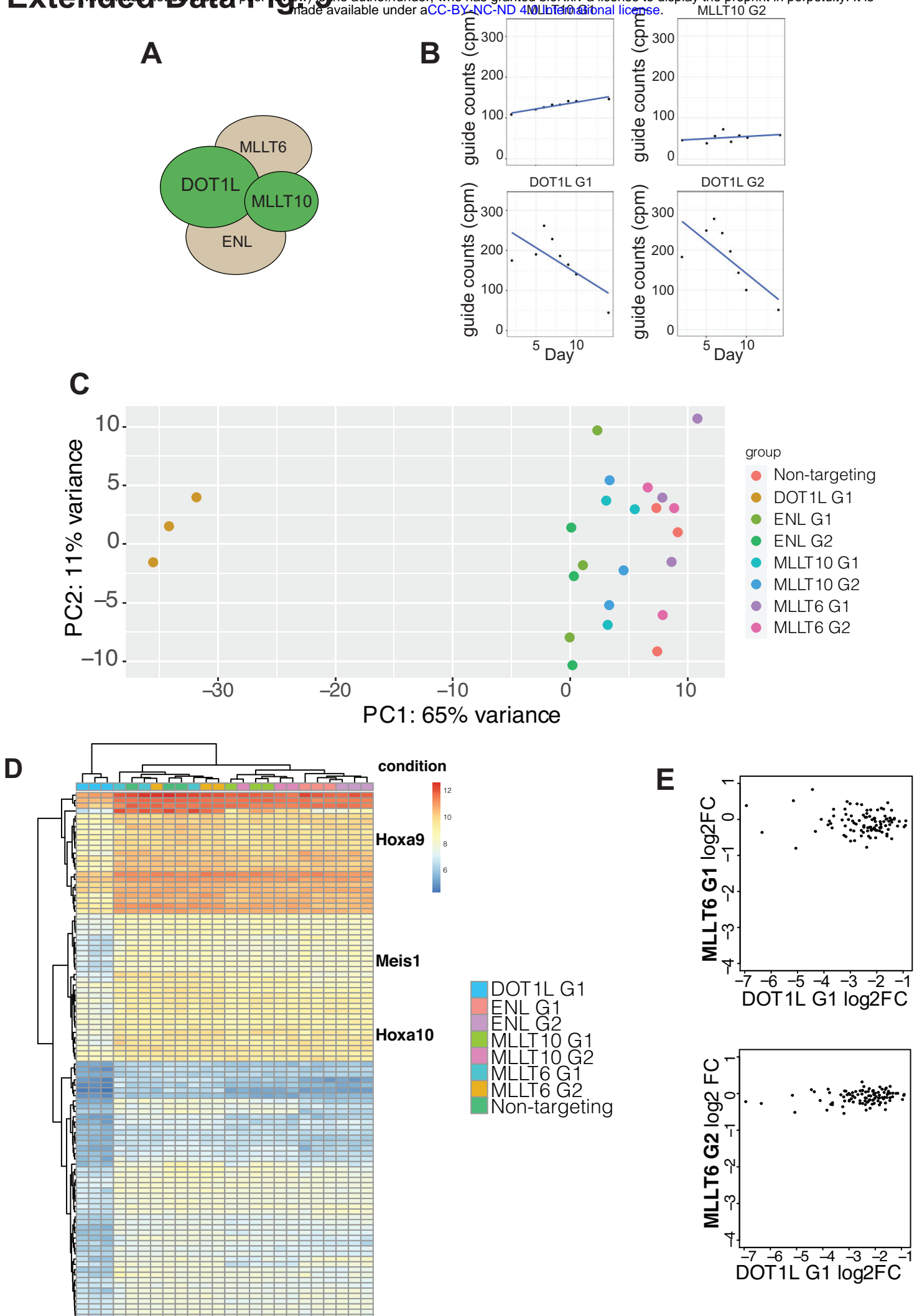
Extended Data Fig. 1

Primer 1 Primer 2

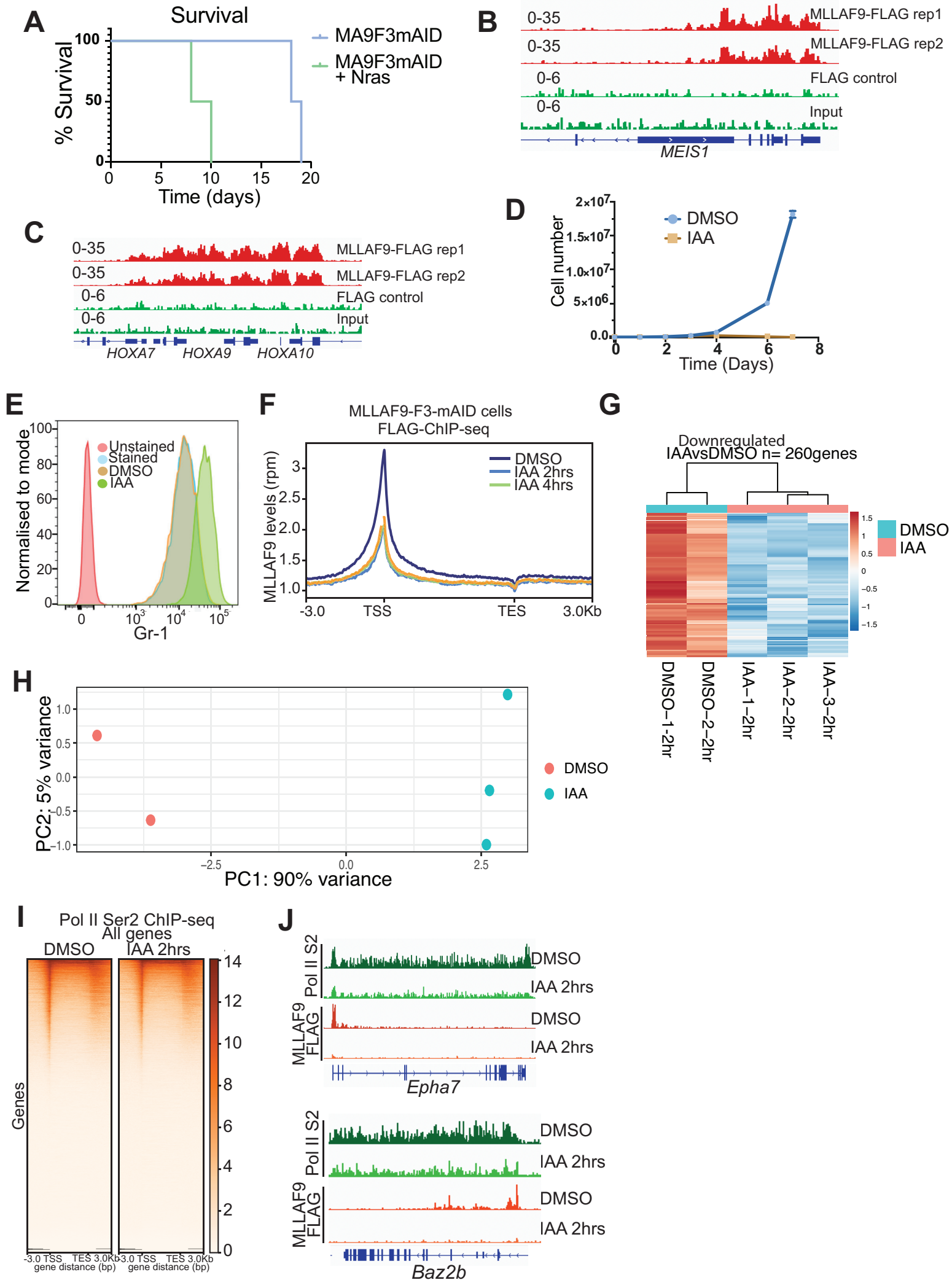




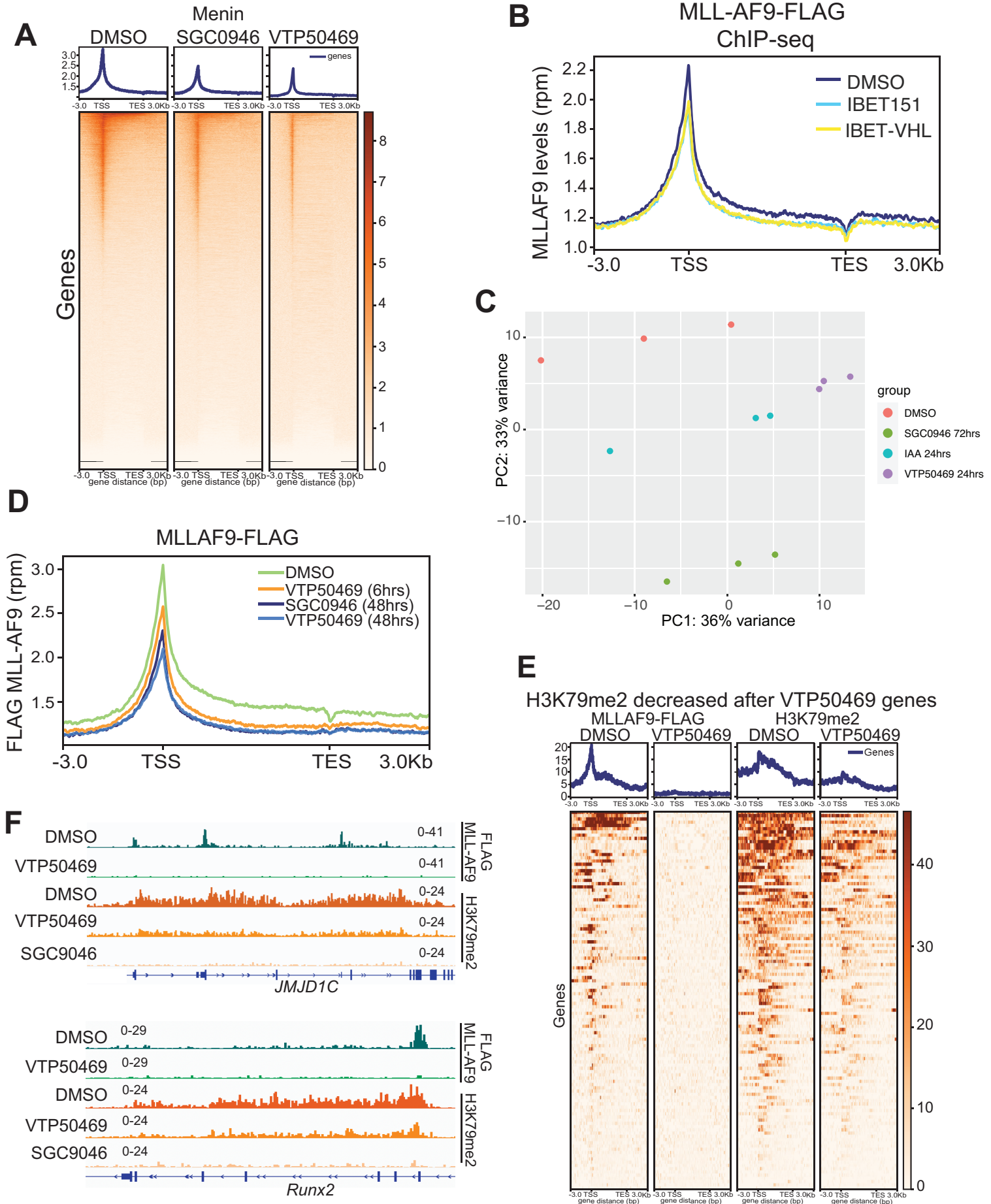
Extended Data Fig. 3



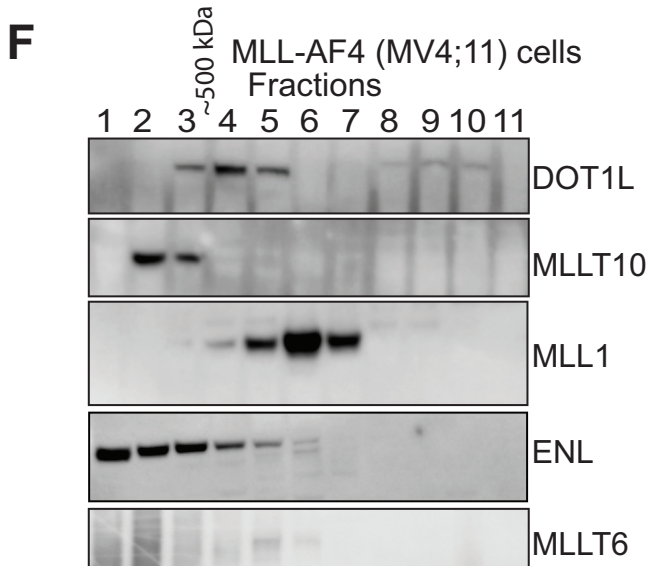
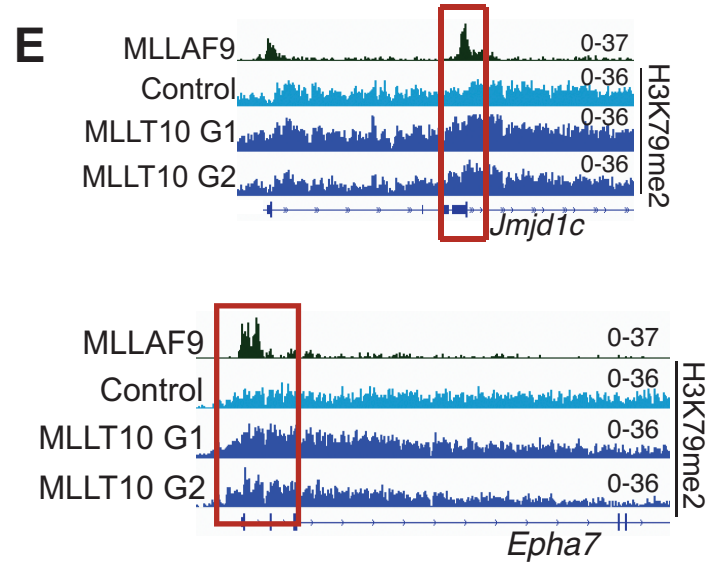
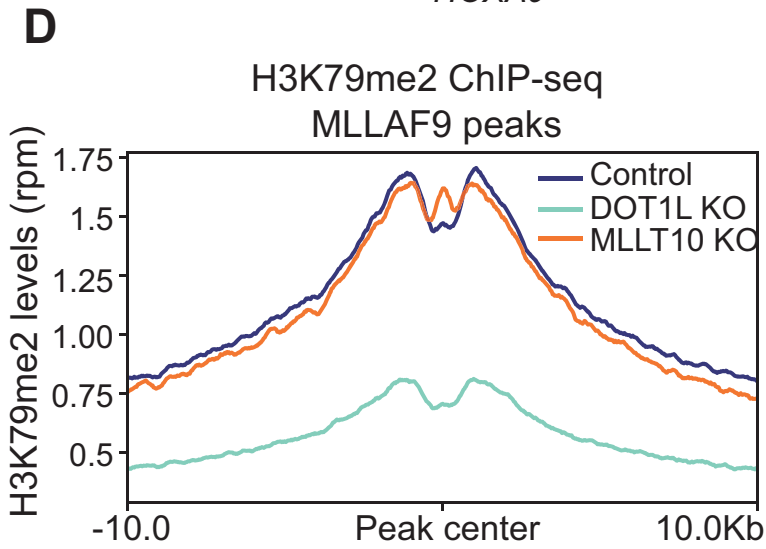
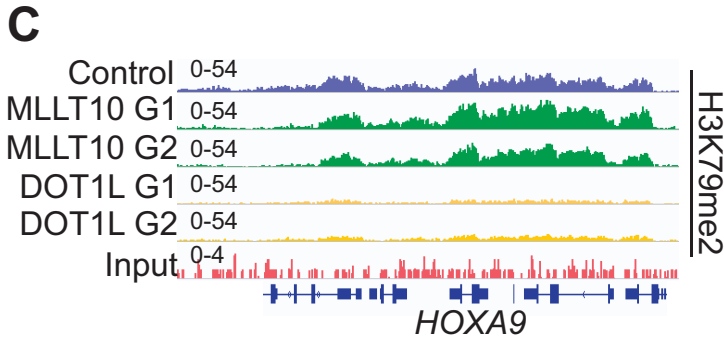
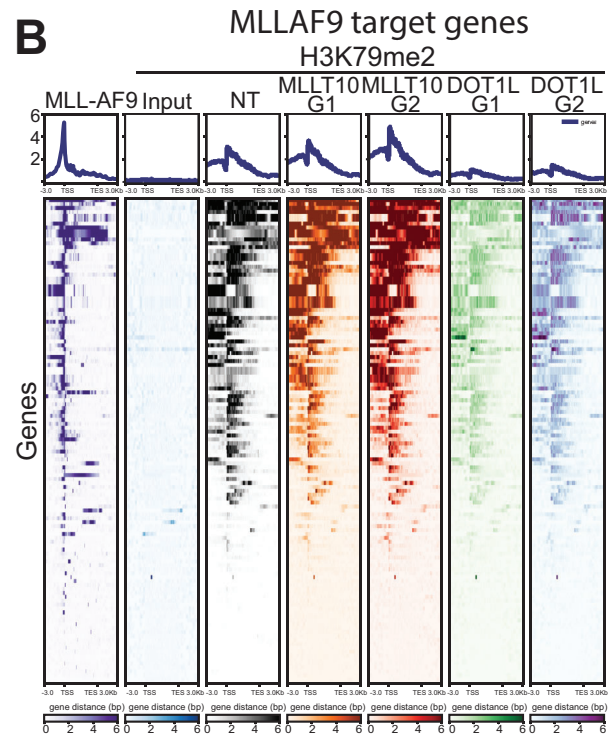
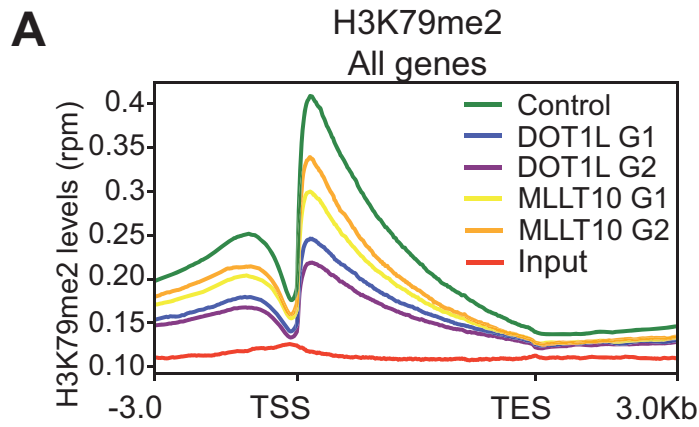
Extended Data Fig. 4



Extended Data Fig. 5



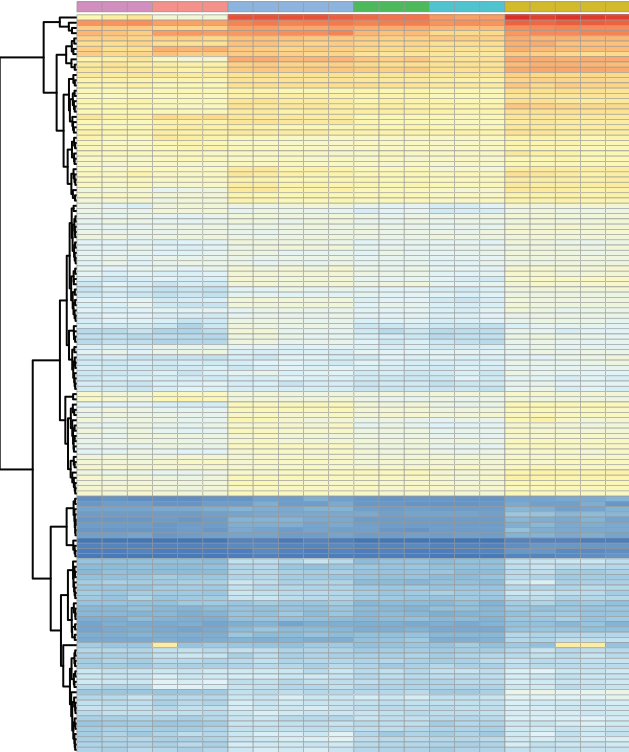
Extended Data Fig. 6



Extended Data Fig. 7

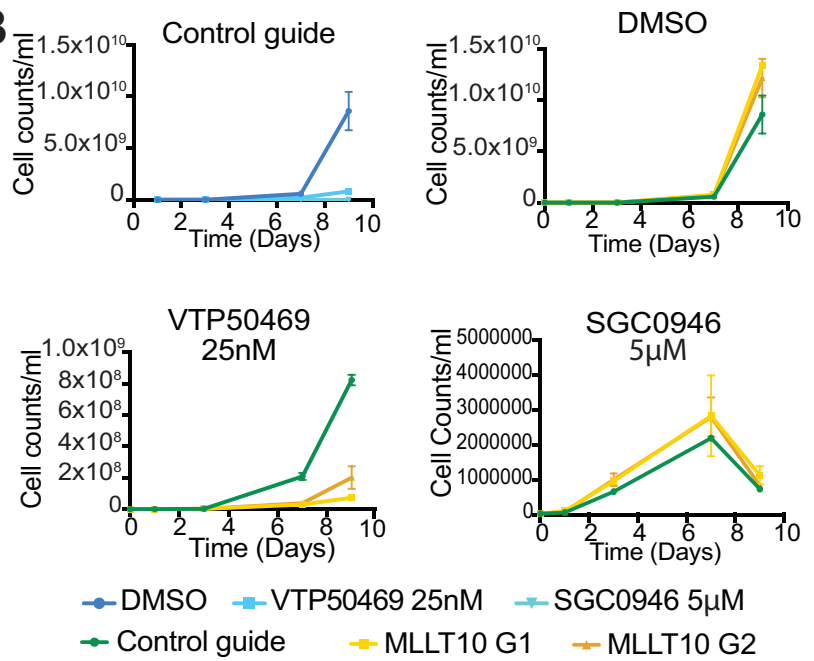
A

MLLT10 KO vs control RNA-seq

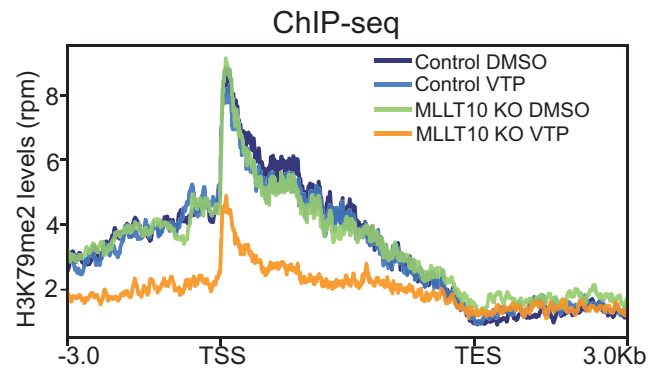


MLLT10 KO 20nM
MLLT10 KO 40nM
MLLT10 KO DMSO
NT 20nM
NT 40nM
NT DMSO

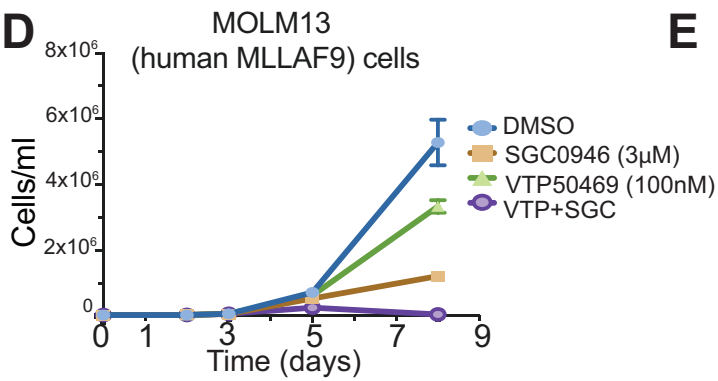
B



C



D



E

